

Reverberation and photoionization estimates of the Broad Line Region Radius in Low- z Quasars

C. Alenka Negrete¹

Instituto Nacional de Astrofísica, Óptica y Electrónica, Mexico

Instituto de Astronomía, Universidad Nacional Autónoma de México, Mexico

Deborah Dultzin²

Instituto de Astronomía, Universidad Nacional Autónoma de México, Mexico

Paola Marziani³

INAF, Astronomical Observatory of Padova, Italy

and

Jack W. Sulentic⁴

Instituto de Astrofísica de Andalucía, Spain

ABSTRACT

Black Hole Mass estimation in quasars, especially at high redshift, involves use of single epoch spectra with s/n and resolution that permit accurate measurement of the width of a broad line assumed to be a reliable virial estimator. Coupled with an estimate of the radius of the broad line region this yields M_{BH} . The radius of the broad line region (BLR) may be inferred from an extrapolation of the correlation between source luminosity and reverberation derived r_{BLR} measures (the so-called Kaspi relation involving about 60 low z sources). We are exploring a different method for estimating r_{BLR} directly from inferred physical conditions in the BLR of each source. We report here on a comparison of r_{BLR} estimates that come from our method and from reverberation mapping. Our “photoionization” method employs diagnostic line intensity ratios in the rest-frame range 1400-2000 Å (AlIII λ 1860/ SiIII λ 1892, CIV λ 1549/AlIII λ 1860) that enable derivation of the product of density and ionization parameter with the BLR

¹cnegrete@inaoep.mx

²deborah@astro.unam.mx

³paola.marziani@oapd.inaf.it

⁴sulentic@iaa.es

distance derived from the definition of the ionization parameter. We find good agreement between our estimates of the density, ionization parameter and r_{BLR} and those from reverberation mapping. We suggest empirical corrections to improve the agreement between individual photoionization-derived r_{BLR} values and those obtained from reverberation mapping. The results in this paper can be exploited to estimate black hole masses M_{BH} for large samples of high- z quasars using an appropriate virial broadening estimator. We show that the width of the UV intermediate emission lines are consistent with the width of $\text{H}\beta$, therefore providing a reliable virial broadening estimator that can be measured in large samples of high- z quasars.

Subject headings: galaxies: active — quasars: general — quasars: emission lines — black holes: physics

1. Introduction

Quasars are intriguing objects whose intense activity arises in a small volume (fraction-of-parsec radius) whose widely accepted interpretation involves accretion onto a central black hole (e.g. D’Onofrio et al. 2012, and references therein). An important signature of a majority of quasars involves the presence of broad emission lines in the UV-optical-IR spectrum. A major challenge involves estimation of the distance r_{BLR} from the central continuum source of the line emitting region (the broad line region: BLR). The BLR cannot be resolved with direct imaging even in the nearest sources. The most direct method for estimating r_{BLR} (hereafter also referred to as the “radius” for brevity) is through reverberation mapping (RM; Peterson 1998; Horne et al. 2004). This technique measures the time delay τ in the response of the broad emission lines to changes in the ionizing continuum. The rest-frame distance is then defined as:

$$r_{\text{BLR}} = \frac{c \cdot \tau}{(1 + z)} = c\tau_{\text{rf}}, \quad (1)$$

where τ_{rf} is the time delay in the quasar rest frame. For brevity we shall use only $c\tau$ to refer to this rest frame distance. r_{BLR} estimates from reverberation mapping require a significant observational effort and have been obtained for only ≈ 50 nearby objects ($z < 0.4$) (Kaspi et al. 2000; Peterson et al. 2004; Kaspi et al. 2005; Bentz et al. 2009, 2010; Denney et al. 2010). An indirect method for measuring r_{BLR} was proposed by Kaspi et al. (2000, 2005) who found a correlation between r_{BLR} and the optical continuum luminosity at 5100\AA ,

$$r_{\text{BLR}} \propto L^\alpha \quad (2)$$

with $\alpha \approx 0.5 - 0.7$ and recent studies favoring a value between 0.5 (Bentz et al. 2009) and 0.6 (Marziani et al. 2009). Apart from uncertainty of the power-law exponent (and any possi-

ble dependence of α on the the luminosity range considered) the rms intrinsic scatter associated with r_{BLR} in the Bentz et al. (2009) data is ≈ 0.28 dex. This method has the advantage of being straightforwardly applicable to large samples of quasars for which single-epoch spectra are available requiring only moderate resolution spectrophotometry involving a broad emission line assumed to be a valid virial estimator. Eq. 2 has paved the way towards definition of “scaling laws” between central black hole mass M_{BH} , line width and luminosity (Shen & Liu 2012, and references therein). Estimating the black hole mass is plagued by large uncertainties because several other variables are at play: emitting region structure, orientation effects, emitting gas dynamics, etc. They will be briefly discussed in §5. However, estimated uncertainties in $\log M_{\text{BH}}$ associated with scaling laws are $\approx \pm 0.3 - 0.4$ dex at 1σ confidence level implying that a large fraction of the scatter is due to the assumption of Eq. 2.

The aim of this paper is to reduce the uncertainty in individual estimates of r_{BLR} and hence M_{BH} . Rather than relying on the $r_{\text{BLR}} - L$ correlation we propose an alternate approach for r_{BLR} estimation based on the simple assumption that gas giving rise to the UV resonance lines is photoionized by the central continuum source. r_{BLR} is then estimated not from a correlation but on an object-by-object basis. The photoionization method is explained in §2, while the sample is described in §3. We compare photoionization and reverberation values in §4. Discussion of the potential advantages are given §4.1. Computations were made considering $H_0 = 70 \text{ km s}^{-1} \text{ Mpc}^{-1}$ and a relative energy density $\Omega_{\Lambda} = 0.7$ and $\Omega_{\text{M}} = 0.3$.

2. Method

The BLR radius r_{BLR} is linked to physical parameters such as hydrogen density (n_{H}) and ionization parameter (U) by the definition of the ionization parameter itself:

$$r_{\text{BLR}} = \left[\frac{\int_{\nu_0}^{+\infty} \frac{L_{\nu}}{h\nu} d\nu}{4\pi n_{\text{H}} U c} \right]^{1/2} \quad (3)$$

where L_{ν} is the specific luminosity per unit frequency ν , h is the Planck constant and c the speed of light. The integral is carried out from the Lyman limit to the largest frequency on the rest frame specific flux $f_{\nu} = L_{\nu}/(4\pi d^2)$. For the integral we will use an average of two Spectral Energy Distributions (SEDs) described by Mathews & Ferland (1987) and Laor et al. (1997). This assumption will be further discussed in §4.1. We can estimate r_{BLR} if we have a reasonable estimate of the product $n_{\text{H}}U$ (Padovani & Rafanelli 1988; Padovani et al. 1990; Negrete 2011; Negrete et al. 2012). Recently, Negrete et al. (2012) (hereafter Paper I) derived n_{H} and U for two high Eddington ratio sources that at low- and moderate L show the typical spectra of narrow-line Seyfert 1s (NLSy1). These findings cannot be easily generalized; however we show in the following that the product $n_{\text{H}}U$ can still be estimated from a set of diagnostic ratios.

2.1. Emission Line Ratios

Emission line ratios such as $\text{CIII}]\lambda 1909 / \text{SiIII}]\lambda 1892$ and $\text{AlIII}\lambda 1860 / \text{SiIII}]\lambda 1892$ are important diagnostics for ranges of density that depend on their transition probabilities (e.g. Feldman et al. 1992). Emission lines originating from forbidden or semi-forbidden transitions become collisionally quenched above the critical density and hence weaker than lines for which collisional effects are negligible. $\text{CIII}]\lambda 1909 / \text{SiIII}]\lambda 1892$ is suitable as a diagnostic when $n_{\text{H}} \lesssim 10^{11} \text{ cm}^{-3}$. The $\text{AlIII}\lambda 1860 / \text{SiIII}]\lambda 1892$ ratio is well suited over the density range $10^{11} - 10^{13} \text{ cm}^{-3}$ (Paper I, Marziani et al. 2011). The ratios $\text{SiII}\lambda 1814 / \text{SiIII}]\lambda 1892$ and $\text{SiIV}\lambda 1397 / \text{SiIII}]\lambda 1892$ are independent of metallicity and sensitive to ionization. The ratio $\text{SiIV}\lambda 1397 / \text{CIV}\lambda 1549$ is mainly sensitive to metallicity. Measuring $\text{SiII}\lambda 1814$ is a challenge in most spectra because of its weakness. Emission line ratios involving $\text{SiII}\lambda 1814$ are therefore subject to large uncertainty and poorly constrain physical conditions. We do not use ratios involving this line. $\text{SiIV}\lambda 1397$ is a stronger line but severe blending with $\text{OIV}]\lambda 1402$ hampers its use. In the extreme sources considered in Paper I the high inferred BC density led us to expect an insignificant $\text{OIV}]\lambda 1402$ contribution. However this might not be true for a more general population of quasars (Wills & Netzer 1979).

We exclude the $\text{SiIV}\lambda 1397 + \text{OIV}]\lambda 1402$ blend and restrict our analysis to three diagnostic ratios involving the four remaining strongest metal lines in the spectra: 1) $\text{CIII}]\lambda 1909 / \text{SiIII}]\lambda 1892$ which is important because several sources show large $\text{CIII}]\lambda 1909$ equivalent widths (unlike sources included in Paper I); 2) $\text{AlIII}\lambda 1860 / \text{SiIII}]\lambda 1892$ that is sensitive to n_{H} and believed to reflect the densest regions which are most optically thick to the ionizing continuum; 3) $\text{CIV}\lambda 1549 / \text{SiIII}]\lambda 1892$ as a marker of ionization level. A quantitative interpretation of these diagnostic ratios requires supporting photoionization simulations. CLOUDY simulations (Ferland et al. 2013) at fixed n_{H} and U values allow us to study how these parameters influence the diagnostic ratios we have adopted. Our simulations span the density range $7.00 \leq \log n_{\text{H}} \leq 14.00$ and $-4.50 \leq \log U \leq 00.00$ in intervals of 0.25 dex assuming plane-parallel geometry, solar metallicity, column density 10^{23} cm^{-2} as well as a “standard” quasar continuum as parameterized by Mathews & Ferland (1987). Further details are given in Paper I. Sources in Paper I show weak $\text{CIII}]\lambda 1909$ emission (relative to $\text{SiIII}]\lambda 1892$) which simplifies interpretation of the emission-line spectrum. In those cases computation of constant value contours for the diagnostic ratios in the U vs. n_{H} plane show convergence towards a low ionization plus high density range. In the case of the sources considered here we show that $\text{AlIII}\lambda 1860 / \text{SiIII}]\lambda 1892$ and $\text{CIV}\lambda 1549 / \text{SiIII}]\lambda 1892$ along with any other ratio not involving $\text{CIII}]\lambda 1909$ converge towards a low-ionization, high n_{H} region while ratios involving $\text{CIII}]\lambda 1909$ converge to a higher ionization, low n_{H} zone (§4).

In the photoionization computations with CLOUDY we have made several simplifying assumptions. The main one consists in deriving a single value of r_{BLR} from fixed physical conditions. It is known that the BLR is not a shell nor a sequence of nested shells; however a gradient of ionization is indicated by the shorter reverberation time responses of lines coming from ions of higher ionization potential (e.g., Peterson & Wandel 1999; Netzer 2008). The r_{BLR} values derived here are probably biased towards the inner radius of the BLR. This is likely to be true for both our method

and the RM because gas close to the continuum source responds more strongly to the incoming ionizing radiation. The $\text{AlIII}\lambda 1860$, $\text{SiIII}]\lambda 1892$, $\text{CIV}\lambda 1549$ lines are all emitted in the fully ionized zone of emitting gas clouds or slabs (Paper I), so that they are sensitive to the ionizing photon flux which is exactly the product $n_{\text{H}}U$. A more realistic approach would be to consider a model that allows gas density n_{H} , column density N_{c} , and ionization parameter U , to be functions of r (Devereux 2013; Devereux & Heaton 2013). As pointed out by Devereux (2013) the r_{BLR} derived from reverberation mapping is an abstraction that may not have a clear structural counterpart, and the RM r_{BLR} can indeed be lower than an emissivity weighted average if the geometry of the BLR is thick (Netzer 1990). Nonetheless, RM r_{BLR} has been considered as the best approximation available for the “virial radius” of the BLR and widely employed as such (e.g. Dultzin-Hacyan et al. 2006; Marziani & Sulentic 2012; Shen 2013, and references therein). Our approach is probably good enough to provide estimate of the “virial radius” equivalent to the one based on RM. In addition, in Paper I we show that our method allows to solve for n_{H} , U and metal content in NLSy1 sources that are $\approx 10\%$ of all quasars.

2.2. Extraction of the Broad Component

Step 1 of our method involves isolation of the broad component (BC) in the selected emission lines. The BC is believed to be associated, at least in part, with the region predominantly emitting low ionization lines (LILs) such as $\text{MgII}\lambda 2800$, FeII , part of the Balmer lines, $\text{SiII}\lambda 1814$, $\text{OI}\lambda 1304$, $\text{CaII}\lambda 8579$ as well as intermediate ionization lines such as $\text{CIII}]\lambda 1909$, $\text{AlIII}\lambda 1860$ and $\text{SiIII}]\lambda 1892$ (Baldwin et al. 2004; Matsuoka et al. 2008; Marziani et al. 2010; Negrete et al. 2012). A BC is present in the overwhelming majority of Seyfert 1 and Type 1 quasar spectra. In order to isolate this component in UV lines we use $\text{H}\beta$ BC to define a BC profile shift and width. We take advantage of the fact that the BC is the dominant component in all LILs if $\text{FWHM}(\text{H}\beta) \lesssim 4000 \text{ km s}^{-1}$ (Population A, Zamfir et al. 2010). We will use the definition of Population A (with a $\text{FWHM}(\text{BC}) \lesssim 4000 \text{ km s}^{-1}$ and Lorentzian BC profile) and Population B (with a $\text{FWHM}(\text{BC}) > 4000 \text{ km s}^{-1}$ and Gaussian BC profile) objects as well as the Eigenvector 1 (E1) parameter space described in Paper I and Sulentic et al. (2000a). In Population A sources $\text{CIV}\lambda 1549$ is often dominated by blueshifted emission probably associated with a high-ionization outflow (Richards et al. 2002; Sulentic et al. 2007). In order to extract BC $\text{CIV}\lambda 1549$ we assume that the broad profile of $\text{CIV}\lambda 1549$ can be described as the sum of the BC (assumed FWHM equal or larger than $\text{FWHM H}\beta$) + a blueshifted component (Marziani et al. 1996; Leighly 2000; Marziani et al. 2010). This approach is further supported by recent work indicating that virial and outflow motions can coexist in quasars (Richards et al. 2011; Wang et al. 2011). For broader (Population B) sources $\text{H}\beta$ can be modeled as the sum of BC and redshifted very broad components (VBC; $\text{FWHM} \sim 10000 \text{ km s}^{-1}$; as in the spectrum of PG0052+251 shown in Fig. 1). For both populations, we fit $\text{CIII}]\lambda 1909$ with the same components of $\text{H}\beta$. In the case of $\text{SiIII}]\lambda 1892$, $\text{AlIII}\lambda 1860$ and $\text{SiII}\lambda 1814$, we fit a single BC component. The sum of the three components (broad, blue-shifted, very-broad) reproduce the line profiles of the strongest lines in low- z quasars (Sulentic et al. 2000b; Marziani

et al. 2010). The relative intensity is different in the various line components but shifts and widths are roughly consistent for all lines. More details are given by Marziani et al. (2010) where line component trends along the E1 sequence are shown.

In practice we apply a multi-component profile decomposition using IRAF task SPECFIT in order to extract the broad line component (Marziani et al. 2010): 1) a relatively unshifted, symmetric BC component representative gas whose broadening is assumed to arise in a virial velocity field. Our aim is to isolate the BC from 2) a blueshifted component associated with outflow or wind emission and 3) a VBC whose strength relative to the BC is set by an inflection observed in the $H\beta$ profile.

3. The Sample of Sources with r_{BLR} Obtained by Reverberation

Reverberated sources allow the product $n_{\text{H}}U$ to be independently estimated from r_{BLR} and the source luminosity by inverting Eq. 3 or, almost equivalently, r_{BLR} derived from photoionization consideration can be directly compared to $c\tau$. We selected 13 of 35 AGN with reverberation data (Peterson et al. 2004, henceforth P04) showing high enough S/N in the rest-frame range 1400-2000 Å to allow accurate decomposition of $\text{CIII}] \lambda 1909$, $\text{SiIII}] \lambda 1892$, $\text{AlIII} \lambda 1860$, and $\text{CIV} \lambda 1549$. We extracted UV spectra from the HST archive and carried out data reduction using standard IRAF tasks. Optical spectra were taken from Marziani et al. (2003). Data were corrected for Galactic extinction. Table 1 presents the sample with IDs given in Column 1 and other columns described below. The redshift of this sample is $z < 0.24$, but the luminosity range is relatively large ($\lambda L_{\lambda}(5100) \sim 10^{43} - 10^{45} \text{ erg s}^{-1}$) and almost uniformly covered.

4. Results

Figure 1 shows the spectra of Pop. A and Pop. B objects; see Col. (2) of Table 1. Fits to Pop. A sources yield line intensities of: a) $\text{CIV} \lambda 1549$ BC + narrow component (NC) + blue-shifted component; b) the 1900Å blend that includes $\text{CIII}] \lambda 1909$ BC, $\text{SiIII}] \lambda 1892$ BC, $\text{AlIII} \lambda 1860$ BC and $\text{SiII} \lambda 1814$ BC; and (c) $H\beta$ BC. Narrow components are fitted whenever clearly visible. For Pop. B sources, the fits yield line intensities of a) $\text{CIV} \lambda 1549$ BC + NC + blue-shifted + VBC; b) 1900Å blend that includes $\text{CIII}] \lambda 1909$ BC + VBC, $\text{SiIII}] \lambda 1892$ BC, $\text{AlIII} \lambda 1860$ BC and $\text{SiII} \lambda 1814$ BC; and c) $H\beta$ BC + NC + VBC. In Table 1, Col. (3) lists the rest-frame specific continuum flux at 1700Å, Cols. (4) to (7) are the rest-frame line flux of the BC components of $\text{CIV} \lambda 1549$, $\text{AlIII} \lambda 1860$, $\text{SiIII}] \lambda 1892$ and $\text{CIII}] \lambda 1909$, Col. (8) is the FWHM of the $H\beta$ BC, Col. (9) is the FWHM of $\text{SiIII}] \lambda 1892$, $\text{AlIII} \lambda 1860$ and of the $\text{CIV} \lambda 1549$ BC. Col. (10) is the dispersion in the FWHM of the BCs. Figure 1 indicates that a BC whose width is consistent with $H\beta$ can be straightforwardly extracted from the $\text{AlIII} \lambda 1860$, and $\text{SiIII}] \lambda 1892$ lines. The same approach yields also the BC component of $\text{CIV} \lambda 1549$.

Armed with line intensities of the BC components we can compute line ratios $\text{AlIII} \lambda 1860 /$

SiIII] λ 1892, CIV] λ 1549/AlIII] λ 1860 (or SiIII] λ 1892) and CIII] λ 1909/ SiIII] λ 1892. These values allow us to draw isopleths i. e., curves representing measured values of these ratios in the n_{H} and U plane. The left panels of Figure 2 show the isocontour maps based on line ratios for SiIII] λ 1892, AlIII] λ 1860 and CIV] λ 1549 emission lines. The right panels show isocontours maps based on line ratios for CIII] λ 1909, SiIII] λ 1892 and CIV] λ 1549. The crossing points give us best estimates of n_{H} and U in the BC of each source. Table 2 lists the estimated product $n_{\text{H}}U$ for our sources. Col. (2) is the product derived from the reverberation mapped data (obtained extracting the product $n_{\text{H}}U$ from Eq. 3 with the assumption $r_{\text{BLR}} = c\tau$), Col. (3) is our estimation derived from the high density solution (left panels of Fig. 2), while Col. (4) is our estimation derived from the low density solution (right panels of Fig. 2). Col. (5) lists $n_{\text{H}}U$ corrected because of systematic effects, as described in §4.1.

CIII] λ 1909 is a semiforbidden line with critical electron density $n_e \sim 10^{10} \text{ cm}^{-3}$ (Osterbrock & Ferland 2006). This density is usually lower than the value found from the diagnostic ratios based on BC components of the UV lines. This means that either CIII] λ 1909 is weak or that it is not produced in the same region. If CIII] λ 1909 is very weak there would be no ambiguity since there is only one solution that is possible: a low U , high n_{H} at the crossing points AlIII] λ 1860/ SiIII] λ 1892, CIV] λ 1549/AlIII] λ 1860. Negrete et al. (2012) have shown that in this case other line ratios (SiII] λ 1814/ SiIII] λ 1892, SiIV] λ 1397/CIV] λ 1549, SiIII] λ 1892/SiIV] λ 1397) support this solution. This emitting region is expected to produce little or no CIII] λ 1909. CIII] λ 1909 traces emission from lower density gas that can also emit SiIII] λ 1892, CIV] λ 1549, and other lines. All contribute to the BC line profile since the emitting region is unresolved. Even if CIII] λ 1909 \approx SiIII] λ 1892 it is possible to predict a correction to the line fluxes and compute ratios that are meant to be free of the low-density gas emission (Negrete 2011; Marziani et al. 2011). If CIII] λ 1909 \gtrsim SiIII] λ 1892 this approach is not possible. Fig. 1 shows that CIII] λ 1909 is prominent in all of our sources. From the crossing points between AlIII] λ 1860/ SiIII] λ 1892 and CIV] λ 1549/ SiIII] λ 1892 on the one hand, and between CIV] λ 1549/ SiIII] λ 1892 and CIII] λ 1909/ SiIII] λ 1892 on the other we derive two mutually exclusive solutions.

In Figure 2 we show isopleth diagrams in the $\log U$ vs. $\log n_{\text{H}}$ plane. In the right panels of Figure 2 we show the solution for a low density emitting region, involving the CIII] λ 1909/ SiIII] λ 1892 ratio. In the left panels we present the high density emitting region solution that includes the AlIII] λ 1860/ SiIII] λ 1892 ratio. Table 2 compares values obtained from the AlIII] λ 1860/ SiIII] λ 1892 and CIII] λ 1909/ SiIII] λ 1892 solution. The AlIII] λ 1860/ SiIII] λ 1892 solution closely corresponds to the one derived from RM extracting the product $n_{\text{H}}U$ from Eq. 3. The average $\log n_{\text{H}}U$ is different by only 0.1 dex in the two cases. The AlIII] λ 1860/ SiIII] λ 1892 values tightly cluster around the average (9.86) with a dispersion of just 0.23 dex, not much larger than the typical uncertainty in individual $\log n_{\text{H}}U$ measures. The distribution of $\log n_{\text{H}}U$ from the CIII] λ 1909/ SiIII] λ 1892 is significantly offset, with average ≈ 8.0 .

We can therefore draw two conclusions: 1) the CIII] λ 1909/ SiIII] λ 1892 ratio is not representative of gas responding to the continuum changes. As mentioned, the CIII] λ 1909 emitting gas must

be in a lower density region whose extent and location is, at present, a matter of guesswork (conceivable scenario may involve low density tails trailing dense clouds, Maiolino et al. 2010, although a larger distance of the CIII]λ1909 emitting gas seems more likely, as inferred below); 2) the high density solution derived from AlIIIλ1860/ SiIII]λ1892 is more representative of the reverberating gas. The uncorrected AlIIIλ1860/ SiIII]λ1892 solution offers a reasonable estimate of the $n_{\text{H}}U$ value derived from RM. The $n_{\text{H}}U(\text{RM})$ and AlIIIλ1860/ SiIII]λ1892 $n_{\text{H}}U$ solutions are uncorrelated. The dispersion for $n_{\text{H}}U(\text{RM})$ values is significantly larger indicating however that there could be a dependence between $n_{\text{H}}U$ estimates and additional parameters.

4.1. Comparison Between r_{BLR} Determinations

As mentioned, the RM sample has the advantage that r_{BLR} is independently known from reverberation. The $n_{\text{H}}U$ and r_{BLR} values are related rewriting Eq. 3 as Eq. 8 of Paper I:

$$r_{\text{BLR}} \approx 93 \left[\frac{f_{\lambda_0, -15} \tilde{Q}_{\text{H}, 0.01}}{(n_{\text{H}}U)_{10}} \right]^{\frac{1}{2}} \zeta(z, 0.3, 0.7) \text{ lt} - \text{days}. \quad (4)$$

where $\lambda_0 = 1700\text{\AA}$, $f_{\lambda_0, -15}$ is the specific rest frame flux (measured on the spectra) in units of $10^{-15} \text{ erg s}^{-1} \text{ cm}^{-2} \text{ \AA}^{-1}$, the product $n_{\text{H}}U$ is normalized to 10^{10} cm^{-3} and r_{BLR} is now expressed in units of light days. Note that $\int_0^{\lambda_{\text{Ly}}} f_{\lambda} \lambda d\lambda = f_{\lambda_0} \cdot \tilde{Q}_{\text{H}}$ with $\tilde{Q}_{\text{H}} = \int_0^{\lambda_{\text{Ly}}} \tilde{s}_{\lambda} \lambda d\lambda$, where \tilde{Q}_{H} depends only on the shape of the ionizing continuum for a given specific flux, and the integral is carried out from the Lyman limit to the shortest wavelengths. ζ is an interpolation function for radial comoving distance as a function of redshift (given by Sulentic et al. 2006) with $\Omega_M = 0.3$ and $\Omega_{\Lambda} = 0.7$. We use the Spectral Energy Distributions (SEDs) \tilde{s}_{λ} by Mathews & Ferland (1987) and by Laor et al. (1997) that have been conveniently parameterized as a set of broken power-laws. \tilde{Q}_{H} is $\approx 0.00963 \text{ cm}\text{\AA}$ and ≈ 0.02181 in the case of the Laor et al. (1997) and Mathews & Ferland (1987) continuum respectively. We use an average \tilde{s}_{λ} value, since the derived $n_{\text{H}}U$ through the photoionization maps is not sensitive to the two different shapes to a first approximation.¹

Using Eq. 4 to compute r_{BLR} for the low- and high-ionization solution, the differences in r_{BLR} between the two cases confirm that the BLR is stratified, with CIII]λ1909 likely emitted at a much larger distance (as indicated in Cols. 7 and 8 of Table 2 and by reverberation studies; see also the recent analysis of NGC 5548 by Kollatschny & Zetzl 2013). The low-density BLR zone is therefore not responding to continuum changes on the same time-scale of Hβ. Hence, the r_{BLR} derived for the high density region is the one that we shall use for any further comparison with the r_{BLR} derived from reverberation of the Hβ emission line. The r_{BLR} derived from the high-density

¹Since the Laor et al. (1997) continuum produces fewer ionizing photons, the same value of U is obtained at a smaller distance. However, the $n_{\text{H}}U$ values are, to a first approximation, independent on the frequency distribution of the ionizing photons in the two SEDs considered.

photoionization solution based on the $\text{AlIII}\lambda 1860/\text{CIII}\lambda 1909$ ratio will be denoted as $r_{\text{BLR},\Phi}$ in what follows.

In Fig 3 we display the residuals $\Delta \log r_{\text{BLR}} = \log r_{\text{BLR}} - \log c\tau$ between the distance computed with four different methods and the reverberation based distance. In Fig. 3 upper left we show the distribution of the $\Delta \log r_{\text{BLR}}$ difference between the photoionization and the reverberation distance, as reported in Cols. (6) and (7) of Table 2. From this figure, we see that the agreement between $\log r_{\text{BLR},\Phi}$ and $\log c\tau$ is good with an average of $\overline{\Delta \log r_{\text{BLR}}} \approx 0.07 \pm 0.29$ dex with a significant scatter. In only two cases (Fairall 9 and NGC 7469) a t -test indicates a significant difference between the two methods.

We use the values of λL_{λ} (5100\AA) and the $\text{H}\beta$ time lags given by Bentz et al. (2009) for the 13 objects of this paper which are included in their sample. We obtain:

$$\log r_{\text{BLR}}(L) \approx -(9.91 \pm 0.34) + (0.61 \pm 0.02) \log \lambda L_{\lambda}(5100\text{\AA}) \quad (5)$$

with residuals -0.01 ± 0.20 dex (Fig. 3 upper right).

For the sample with RM data of ≈ 50 objects, Bentz et al. (2009) derive the equation

$$\log R_{\text{BLR}}(L) = -21.3 + 0.519 \log \lambda L_{\lambda}(5100\text{\AA}) \quad (6)$$

If we apply this correlation to our sample (Fig. 3 lower left) we obtain a residual rms ± 0.20 dex but with a significant bias (-0.09 dex) that makes the uncertainty again ≈ 0.3 dex, as also indicated by the full sample of Bentz et al. (2009). Therefore $r_{\text{BLR},\Phi}$ estimates show precision and accuracy that are similar to the ones based on the luminosity correlation of Bentz et al. (2009). In our case the luminosity correlation of Bentz et al. (2009) systematically over-predicts r_{BLR} by $\Delta \log r_{\text{BLR}} \approx 0.1$ dex, as shown also in Fig. 3 lower left.

The formal median uncertainty at 1σ confidence level is ± 0.1 dex in R_{BLR} for RM (Fig. 3 lower left), and comparable to the photoionization method (Fig. 3 upper right). If the RM values are assumed to be the “true” r_{BLR} values, the photoionization method (in its simplest formulation) yields information that is not accurate in 2 of 13 cases, as mentioned above. Its precision is comparable to the luminosity correlation.

4.2. Analysis of Systematic Differences

Emission line ratios used for the computation of the high density solution are most likely affected by lower density $\text{CIII}\lambda 1909$ emission. Therefore, we expect that any disagreement between $n_{\text{H}}U$ might be influenced by the equivalent widths and the relative strength of the emission lines considered, and especially by the prominence of $\text{CIII}\lambda 1909$.

Three correlations emerge from the consideration of the residuals $\Delta \log n_{\text{H}}U = \log n_{\text{H}}U(\Phi) - \log n_{\text{H}}U(\text{RM})$, where we have again conventionally indicated with $n_{\text{H}}U(\Phi)$ the solution based on the $\text{Al III } \lambda 1860 / \text{Si III } \lambda 1892$ ratio. The $n_{\text{H}}U(\text{RM})$ is derived from Eq. 4 using $c\tau$ from reverberation. Figure 4 presents comparisons of $\Delta \log n_{\text{H}}U$ as a function of luminosity, and the equivalent widths of $\text{C III } \lambda 1909$, $\text{Si III } \lambda 1892$ and $\text{Al III } \lambda 1860$. Errors on line intensity (computed considering continuum level uncertainty) are quadratically propagated to compute errors for the diagnostic ratios and hence for the product $n_{\text{H}}U$. Best fit lsq solutions are as follows:

$$\Delta \log n_{\text{H}}U \approx (1.49 \pm 0.05) \log \lambda L_{\lambda}(5100\text{\AA}) - (65.76 \pm 2.39). \quad (7)$$

$$\Delta \log n_{\text{H}}U \approx (-4.29 \pm 0.45) \log W(\text{C III } \lambda 1909) + (5.73 \pm 0.43) \quad (8)$$

$$\Delta \log n_{\text{H}}U \approx (-2.98 \pm 0.27) \log W(\text{Si III } \lambda 1892) + (3.28 \pm 0.43) \quad (9)$$

$$\Delta \log n_{\text{H}}U \approx (-3.00 \pm 0.66) \log W(\text{Al III } \lambda 1860) + (1.98 \pm 0.87) \quad (10)$$

The equations of this section yielding a correction for $\log n_{\text{H}}U$ as a function of equivalent widths can be used to recompute r_{BLR} . This operation would eliminate any bias between $n_{\text{H}}U(\Phi)$ and $n_{\text{H}}U(\text{RM})$ estimates but the scatter in the r_{BLR} residuals computed after applying a correction would remain large, ≈ 0.3 dex. A similar scatter is obtained if a correction is defined directly correlating $\Delta \log r_{\text{BLR}}$ against the equivalent widths of $\text{C III } \lambda 1909$, $\text{Si III } \lambda 1892$ and $\text{Al III } \lambda 1860$. It is perhaps not surprising that the scatter is not reduced since equivalent widths are expected to be influenced by several factors affecting the gas physical conditions (i.e., continuum luminosity, covering factor, etc.). We can improve the correction if we use the ratios of line equivalent widths or fluxes, as shown below.

4.2.1. Improving the Agreement

The relation between $\log c\tau$ vs. $\log r_{\text{BLR},\Phi}$ (Figure 5 upper panel) is given by

$$\log c\tau \approx (1.16 \pm 0.07) \log r_{\text{BLR},\Phi} - (2.74 \pm 0.40) \quad (11)$$

The Pearson correlation coefficient is $R \approx 0.82$, implying probability $P \approx 0.003$ for the correlation to occur by chance. This equation yields an $\text{rms} \approx 0.30$ dex, a value similar to the scatter in r_{BLR} values obtained through the correlation with luminosity.

In order to obtain an even better correlation, we apply a correction using the equivalent width ratio $W(\text{AlIII}\lambda 1860)/W(\text{CIII}\lambda 1909)$ that is more effective (Fig. 5 middle panel):

$$\log r_{\text{BLR},\Phi} - \log c\tau \approx (1.06 \pm 0.25) \log \frac{W(\text{AlIII}\lambda 1860)}{W(\text{CIII}\lambda 1909)} + (0.81 \pm 0.26) \quad (12)$$

The correlation coefficient is 0.62 which for 12 objects implies a marginal significance slightly over a 2σ confidence level. Fig. 3(lower right) shows a somewhat more compact distribution in the $\Delta \log r_{\text{BLR}}$ values. There is one outlying source that has been excluded from the analysis, PG 0953+414. This source shows considerable narrow absorption that appear to significantly eat away part of the $\text{CIII}\lambda 1909$ line, making an estimate of the $W(\text{AlIII}\lambda 1860)/W(\text{CIII}\lambda 1909)$ ratio rather difficult.

The correlation of $r_{\text{BLR},\Phi}$ corrected and $c\tau$ is (Fig. 5 lower panel):

$$\log r_{\text{BLR},\Phi_{\text{corr}}} \approx (0.77 \pm 0.14) \log c\tau + (3.94 \pm 0.75) \quad (13)$$

with a scatter of ≈ 0.23 dex and a correlation coefficient of 0.89. The absence of a significant bias in the corrected $r_{\text{BLR},\Phi}$ comes from the definition of the correlation on the present sample. However, since $r_{\text{BLR},\Phi}$ is computed on an object by object basis it is reasonable to assume that no bias will be introduced in different samples. The photoionization method is therefore expected to be also somewhat more accurate than the luminosity correlation.

5. Discussion

The preceding sections showed that the photoionization method used in this paper is yielding physically meaningful values, that are consistent with r_{BLR} derived from reverberation mapping. Values of r_{BLR} derived from photoionization arguments are known to be consistent with $c\tau$. A similar method assuming a constant $n_{\text{H}}U$ also provides consistent agreement (Padovani et al. 1990; Padovani & Rafanelli 1988; Wandel et al. 1999; see also Chapter 4 of D’Onofrio et al. 2012). A reassessment of the method of Dibai (1977) based on the luminosity of Balmer line shows agreement with reverberation derived masses within ± 0.3 dex (Bochkarev & Gaskell 2009).

The agreement between photoionization results and the correlation with luminosity is expected since the diagnostic ratios measure the product $n_{\text{H}}U$ that is the ionizing photo flux. If the correction provided by Eq. 12 is valid in general, then the photoionization method can provide a significant improvement in precision for single epoch r_{BLR} estimates, lowering the dispersion around RM-derived r_{BLR} from more than a factor 2 (if the luminosity correlation is used) to $\approx 70\%$.

5.1. Influence of Continuum

We adopted a very simplified approach, that neglects (1) the diversity in the ionizing continua among sources, and (2) the dependence of $n_{\text{H}}U$ on ionizing continuum shape. It is unlikely that, with the chosen simplified approach, a better agreement between photoionization and RM r_{BLR} estimates can be achieved. First, r_{BLR} from RM is subject to a significant uncertainty, and shapes of the cross-correlation function are not always regular. Second, a significant part of the scatter is associated to the assumption of an average SED. Using the SEDs of each individual source, and repeating the photoionization simulation array that defines $n_{\text{H}}U$ should lead to a significant improvement. The simplified approach is meant to make the method easily applicable to high- z quasars for which SEDs data are most often unavailable at present.

5.2. Interpretation of the Empirical Correction

Eq. 12 needs to be confirmed by more extended data. It is based on an heterogeneous sample of 12 objects only. Physical properties within the BC are not found to be identical across the E1 sequence. In principle, Eq. 12 should be built separating the most populated spectral types along E1. This feat is however beyond the possibilities offered by available data. Given the unclear role of continuum diversity, it is not easy to derive a unique physical interpretation beyond the following qualitative considerations. Eq. 12 indicate that $r_{\text{BLR}}(\Phi)$ for smaller $\text{AlIII}\lambda 1860/\text{CIII}\lambda 1909$ ratio sources significantly under-predicts $c\tau$, while the agreement is better for relatively large $\text{AlIII}\lambda 1860/\text{CIII}\lambda 1909$ ratios. This is consistent with the results of Paper I. Stronger $\text{CIII}\lambda 1909$ emitters (for example PG 1211+143 and PG 1411+442 of spectral type A1 of the E1) may appreciably respond to continuum changes at a systematically larger distance with respect to the denser, low ionization gas. The denser low ionization gas may account for a small fraction of the emitting gas if $\text{CIII}\lambda 1909/\text{AlIII}\lambda 1860 \gg 1$.

5.3. Influence of Continuum Variability

The previous results rely on the assumption that we can take an average AGN ionizing continuum. In fact, however, we know that the continuum is variable and in some cases very variable. When the ionizing continuum varies Eq. 4 predicts a variation in r_{BLR} . The physical reasons for the variation in r_{BLR} may be twofold: a) the ionizing continuum may penetrate farther among the BLR clouds and/or b) the effect of radiation pressure can push the clouds further away. Regardless of the ultimate physical interpretation, we can confront r_{BLR} derived from reverberation mapping and from photoionization in different continuum states. We considered the case of NGC5548 which is a very well monitored object. The lowest and highest value for the flux at $\lambda 1700\text{\AA}$ were retrieved

from the AGN watch website². We then calculated n_{H} and U for the two states. For the lowest value ($0.94 \cdot 10^{-14} \text{erg s}^{-1} \text{cm}^{-2}$), we obtain $n_{\text{H}}U = 9.85$, and for the highest value ($4.78 \cdot 10^{-14} \text{erg s}^{-1} \text{cm}^{-2}$) we obtain $n_{\text{H}}U = 10.04$. These products yield a variation from $\log(r_{\text{BLR}}) = 16.26$ to $\log(r_{\text{BLR}}) = 16.52$. The isopleths indicate that the change in $n_{\text{H}}U$ is driven by a change in U that is affecting strongly $\text{CIV}\lambda 1549$, remaining the n_{H} value almost constant. The r_{BLR} change goes in the same sense of the ones derived from the AGN watch and reported by Bentz et al. (2009) although $c\tau$ seems to be affected more strongly by continuum changes, with a 3-fold increase in r_{BLR} for a 3-fold increase in continuum.

5.4. M_{BH} Computation

Knowing r_{BLR} enables us to estimate the black hole mass (M_{BH}) assuming virial motions of the gas using:

$$M_{\text{BH}} = f \frac{\Delta v^2 r_{\text{BLR}}}{G} = \frac{3}{4G} f_{0.75} \text{FWHM}^2 r_{\text{BLR}} \quad (14)$$

where G is the gravitational constant. If $\Delta v = \text{FWHM}$ of a line, the geometry factor $f = \sqrt{3}/2$ if the orbits of the BLR clouds are randomly oriented. We use $f_{0.75} = 1.4$ (Graham et al. 2011).

As mentioned earlier, the BC of $\text{CIV}\lambda 1549$, $\text{SiIII}]\lambda 1892$, and $\text{AlIII}\lambda 1860$ isolates emission that is believed to come from the same low-ionization region emitting the core of $\text{H}\beta$, and LILs like $\text{MgII}\lambda 2800$, FeII , $\text{SiII}\lambda 1814$. It is believed that the BC broadening is due to Keplerian motions since the BC does not present strong asymmetries or centroid shifts with respect to rest frame. Therefore, use of $\text{AlIII}\lambda 1860$ or $\text{SiIII}]\lambda 1892$ BC FWHM derived from the multicomponent fits should be regarded as “safe” as the use $\text{FWHM}(\text{H}\beta_{\text{BC}})$ for obtaining a BLR velocity dispersion indicator. This is not true for the blue-shifted component and for the VBC. The $\text{CIV}\lambda 1549$ blue-shifted asymmetry found in many quasars is read as the signature of an outflowing wind (Marziani & Sulentic 2012, and references therein). The large shift of the VBC similarly suggests that non-virial motions play a significant role. The low-ionization part of the BLR that should emit the BC we isolated is still prominent in high luminosity quasars (Marziani et al. 2009), and this makes the photoionization method discussed in this paper straightforwardly applicable to high redshift quasars (Negrete et al. in preparation). The RM sample offered the possibility to check that the BC FWHM of $\text{AlIII}\lambda 1860$ and $\text{SiIII}]\lambda 1892$ is indeed consistent with the BC FWHM of $\text{H}\beta$ (last columns of Table 1). $\text{AlIII}\lambda 1860$, $\text{SiIII}]\lambda 1892$ may offer the most consistent FWHM estimators. $\text{CIV}\lambda 1549$ should be avoided unless a detailed analysis as in Figure 1 can be carried since it is often blueward asymmetric. $\text{CIII}]\lambda 1909$ may be significantly narrower than $\text{SiIII}]\lambda 1892$ and $\text{AlIII}\lambda 1860$, and, as stressed, is not associated to the high-density solution. Therefore also $\text{CIII}]\lambda 1909$ FWHM

²<http://www.astronomy.ohio-state.edu/~agnwatch/n5548/spectra>

should be avoided as a virial broadening estimator.

Fig. 6 compares the mass computed from Eq. 14 using r_{BLR} estimated from RM, our photoionization method and two luminosity correlations. As seen for r_{BLR} the agreement is improved if systematic effects are corrected with the $W(\text{AlIII}\lambda 1860)/W(\text{CIII}\lambda 1909)$ relation. The scatter and the bias in the $\text{CIV}\lambda 1549$ luminosity derived masses of Shen et al. (2011) is probably related to significant broadening of the CIV line by non-virial motion (e.g., Netzer et al. 2007; Sulentic et al. 2007). On the contrary, the Vestergaard & Peterson (2006) relationship provides more accurate values since it has been calibrated on a dataset that includes the sources considered in this paper.

5.5. Further Considerations

The assumption of RM values as the true values is a working hypothesis. RM based masses may be accurate to within a factor ≈ 3 (Vestergaard & Peterson 2006), if they are compared to the masses derived from the $M_{\text{BH}} - \text{bulge velocity dispersion}$. However, the origin of this dispersion may include statistical (i.e., orientation) and systematic effects (as the geometry factor f) that do not enter in the r_{BLR} measures. The determination of r_{BLR} on an individual source basis allows an immediate comparison with RM values and to independently consider other systematic and statistical effects involved in the M_{BH} estimate. An average f value for all AGNs is unlikely to be appropriate (as derived from the scaling with the $M_{\text{BH}} - \text{bulge velocity dispersion}$) since the line profiles of the strongest emission lines suggest structural and dynamical changes along the so-called “Eigenvector 1” sequence. Therefore the photoionization method has the potential advantage (unlike methods based on $M_{\text{BH}} - \text{FWHM} - \text{luminosity correlation}$) to “reproduce” RM r_{BLR} values at high redshift, leaving the possibility to consider f and orientation effects on an individual basis.

6. Conclusion

In summary, we are able to estimate BLR distances using an independent photoionization method that yields results consistent with reverberation values for 13 sources in common (Bentz et al. 2009). Although we cannot constrain BLR physical conditions as well as we were able to do for extreme Population A sources (Paper I), we are nonetheless able to derive empirical relations that further improve the agreement between photoionization and RM r_{BLR} determinations. We suggest that the derived r_{BLR} values can significantly improve black hole mass estimation especially at $z \gtrsim 2$ when the intermediate ionization lines are shifted into the wavelength range accessible to optical spectrometers. The width of the broad intermediate ionization lines likely provides a reliable virial estimator leaving the geometry factor f and poorly understood orientation effects as the main sources of uncertainty.

A. Negrete and D. Dultzin acknowledge support from grant IN111610 PAPIIT UNAM, and Yair Krongold for fruitful discussions. JWS acknowledges support under a Proyecto de Excelencia contract from La Junta de Andalucia.

REFERENCES

- Baldwin, J. A., Ferland, G. J., Korista, K. T., Hamann, F., & LaCluyzé, A. 2004, *ApJ*, 615, 610
- Bentz, M. C., Peterson, B. M., Pogge, R. W., & Vestergaard, M. 2009, *ApJL*, 694, L166
- Bentz, M. C., et al. 2010, *ApJ*, 716, 993
- Bochkarev, N. G., & Gaskell, C. M. 2009, *Astronomy Letters*, 35, 287
- Denney, K. D., et al. 2010, *ApJ*, 721, 715
- Devereux, N. 2013, *ApJ*, 764, 79
- Devereux, N., & Heaton, E. 2013, *ArXiv e-prints*
- Dibai, E. A. 1977, *Soviet Astronomy Letters*, 3, 1
- D’Onofrio, M., Marziani, P., & Sulentic, J. W., eds. 2012, *Astrophysics and Space Science Library*, Vol. 386, *Fifty Years of Quasars*
- Dultzin-Hacyan, D., Marziani, P., & Sulentic, J. W. 2006, in *American Institute of Physics Conference Series*, Vol. 861, *Albert Einstein Century International Conference*, ed. J.-M. Alimi & A. Füzfa, 614–621
- Feldman, U., Mandelbaum, P., Seely, J. F., Doschek, G. A., & Gursky, H. 1992, *ApJS*, 81, 387
- Ferland, G. J., et al. 2013, *Rev. Mexicana Astron. Astrofis.*, 49, 137
- Graham, A. W., Onken, C. A., Athanassoula, E., & Combes, F. 2011, *MNRAS*, 412, 2211
- Horne, K., Peterson, B. M., Collier, S. J., & Netzer, H. 2004, *PASP*, 116, 465
- Kaspi, S., Maoz, D., Netzer, H., Peterson, B. M., Vestergaard, M., & Jannuzi, B. T. 2005, *ApJ*, 629, 61
- Kaspi, S., Smith, P. S., Netzer, H., Maoz, D., Jannuzi, B. T., & Giveon, U. 2000, *ApJ*, 533, 631
- Kollatschny, W., & Zetzl, M. 2013, *A&A*, 551, L6
- Laor, A., Fiore, F., Elvis, M., Wilkes, B. J., & McDowell, J. C. 1997, *ApJ*, 477, 93
- Leighly, K. M. 2000, *New A Rev.*, 44, 395

- Maiolino, R., et al. 2010, *A&A*, 517, A47+
- Marziani, P., Alenka Negrete, C., Dultzin, D., & Sulentic, J. W. 2011, *Baltic Astronomy*, 20, 406
- Marziani, P., & Sulentic, J. W. 2012, *New A Rev.*, 56, 49
- Marziani, P., Sulentic, J. W., Dultzin-Hacyan, D., Calvani, M., & Moles, M. 1996, *ApJS*, 104, 37
- Marziani, P., Sulentic, J. W., Negrete, C. A., Dultzin, D., Zamfir, S., & Bachev, R. 2010, *MNRAS*, 409, 1033
- Marziani, P., Sulentic, J. W., Stirpe, G. M., Zamfir, S., & Calvani, M. 2009, *A&Ap*, 495, 83
- Marziani, P., Sulentic, J. W., Zamanov, R., Calvani, M., Dultzin-Hacyan, D., Bachev, R., & Zwitter, T. 2003, *ApJS*, 145, 199
- Mathews, W. G., & Ferland, G. J. 1987, *ApJ*, 323, 456
- Matsuoka, Y., Kawara, K., & Oyabu, S. 2008, *ApJ*, 673, 62
- Negrete, C. A. 2011, PhD thesis, UNAM, Mexico, (2011)
- Negrete, C. A., Dultzin, D., Marziani, P., & Sulentic, J. W. 2012, *ApJ*, 757, 62
- Netzer, H. 1990, in *Active Galactic Nuclei*, ed. R. D. Blandford, H. Netzer, L. Woltjer, T. J.-L. Courvoisier, & M. Mayor, 57–160
- Netzer, H. 2008, *New A Rev.*, 52, 257
- Netzer, H., Lira, P., Trakhtenbrot, B., Shemmer, O., & Cury, I. 2007, *ApJ*, 671, 1256
- Osterbrock, D. E., & Ferland, G. J. 2006, *Astrophysics of gaseous nebulae and active galactic nuclei* (University Science Books)
- Padovani, P., Burg, R., & Edelson, R. A. 1990, *ApJ*, 353, 438
- Padovani, P., & Rafanelli, P. 1988, *A&A*, 205, 53
- Peterson, B. M. 1998, *Advances in Space Research*, 21, 57
- Peterson, B. M., & Wandel, A. 1999, *ApJ*, 521, L95
- Peterson, B. M., et al. 2004, *ApJ*, 613, 682
- Richards, G. T., Vanden Berk, D. E., Reichard, T. A., Hall, P. B., Schneider, D. P., SubbaRao, M., Thakar, A. R., & York, D. G. 2002, *AJ*, 124, 1
- Richards, G. T., et al. 2011, *AJ*, 141, 167
- Shen, Y. 2013, ArXiv e-prints

- Shen, Y., & Liu, X. 2012, *ApJ*, 753, 125
- Shen, Y., et al. 2011, *ApJS*, 194, 45
- Sulentic, J. W., Bachev, R., Marziani, P., Negrete, C. A., & Dultzin, D. 2007, *ApJ*, 666, 757
- Sulentic, J. W., Marziani, P., & Dultzin-Hacyan, D. 2000a, *ARA&A*, 38, 521
- Sulentic, J. W., Repetto, P., Stirpe, G. M., Marziani, P., Dultzin-Hacyan, D., & Calvani, M. 2006, *A&Ap*, 456, 929
- Sulentic, J. W., Zwitter, T., Marziani, P., & Dultzin-Hacyan, D. 2000b, *ApJL*, 536, L5
- Vestergaard, M., & Peterson, B. M. 2006, *ApJ*, 641, 689
- Wandel, A., Peterson, B. M., & Malkan, M. A. 1999, *ApJ*, 526, 579
- Wang, H., Wang, T., Zhou, H., Liu, B., Wang, J., Yuan, W., & Dong, X. 2011, *ApJ*, 738, 85
- Wills, D., & Netzer, H. 1979, *ApJ*, 233, 1
- Zamfir, S., Sulentic, J. W., Marziani, P., & Dultzin, D. 2010, *MNRAS*, 403, 1759

Table 1. Measured quantities

| Object (1) | Pop. type ^a (2) | $f_{\lambda}(1700 \text{ \AA})^b$ (3) | Line Flux ^c | | | | FWHM ^d | | |
|---------------|-------------------------------|--|---------------------------|-----------------------------|-----------------------------|----------------------------|-------------------|-----------|------------------|
| | | | CIV λ 1549 (4) | AlIII λ 1860 (5) | SiIII λ 1892 (6) | CIII λ 1909 (7) | H β (8) | UV (9) | σ (10) |
| AKN120 | B | 8.1 \pm 0.5 | 82.8 $^{+4.1}_{-1.0}$ | 4.7 $^{+2.6}_{-1.3}$ | 13.0 $^{+1.2}_{-1.3}$ | 13.2 $^{+0.6}_{-1.4}$ | 5480 | 4990 | 420 |
| Fairall 9 | B | 3.6 \pm 0.4 | 25.3 $^{+2.5}_{-2.5}$ | 1.4 $^{+0.4}_{-0.4}$ | 4.5 $^{+0.5}_{-0.5}$ | 5.3 $^{+0.5}_{-0.5}$ | 4540 | 4550 | 50 |
| MRK 335 | A | 7.1 \pm 0.7 | 54.8 $^{+5.5}_{-5.5}$ | 1.4 $^{+0.4}_{-0.4}$ | 4.2 $^{+0.5}_{-0.5}$ | 10.6 $^{+1.1}_{-1.1}$ | 1960 | 1870 | 200 |
| MRK 509 | A | 8.9 \pm 0.6 | 116.5 $^{+2.5}_{-3.5}$ | 5.1 $^{+1.6}_{-0.9}$ | 12.5 $^{+2.0}_{-0.5}$ | 20.6 $^{+1.4}_{-1.6}$ | 3390 | 3290 | 300 |
| NGC 3516 | B | 4.7 \pm 0.2 | 49.1 $^{+2.4}_{-2.6}$ | 2.3 $^{+0.6}_{-0.4}$ | 7.5 $^{+0.5}_{-0.3}$ | 7.4 $^{+0.1}_{-0.4}$ | 6530 | 5270 | 700 |
| NGC 3783 | A | 10.9 \pm 0.1 | 106.9 $^{+4.1}_{-2.9}$ | 2.5 $^{+0.9}_{-0.3}$ | 5.9 $^{+1.3}_{-0.1}$ | 17.3 $^{+0.5}_{-0.3}$ | 2870 | 2860 | 100 |
| NGC 5548 | B | 3.1 \pm 0.1 | 51.1 $^{+2.4}_{-1.4}$ | 1.6 $^{+0.5}_{-0.3}$ | 4.3 $^{+0.2}_{-0.2}$ | 7.0 $^{+0.2}_{-0.2}$ | 5820 | 5390 | 330 |
| NGC 7469 | A | 4.7 \pm 0.4 | 57.0 $^{+1.0}_{-1.5}$ | 4.2 $^{+0.8}_{-0.6}$ | 7.8 $^{+0.7}_{-0.4}$ | 12.7 $^{+0.5}_{-0.7}$ | 2850 | 3090 | 210 |
| PG 0052+251 | B | 2.4 \pm 0.1 | 15.0 $^{+0.5}_{-0.2}$ | 0.6 $^{+0.3}_{-0.2}$ | 2.0 $^{+0.3}_{-0.2}$ | 2.7 $^{+0.2}_{-0.1}$ | 5340 | 5240 | 530 |
| PG 0953+414 | A | 1.9 \pm 0.1 | 16.8 $^{+0.4}_{-0.5}$ | 1.0 $^{+0.1}_{-0.2}$ | 1.0 $^{+0.3}_{-0.2}$ | 2.8 $^{+0.2}_{-0.6}$ | 3390 | 3520 | 210 |
| PG 1211+143 | A | 2.9 \pm 0.1 | 25.0 $^{+0.8}_{-0.7}$ | 0.6 $^{+0.3}_{-0.2}$ | 1.6 $^{+0.2}_{-0.3}$ | 3.9 $^{+0.3}_{-0.2}$ | 2440 | 2350 | 280 |
| PG 1307+085 | B | 1.6 \pm 0.1 | 111.8 $^{+7.2}_{-4.7}$ | 3.4 $^{+2.1}_{-1.2}$ | 10.8 $^{+2.3}_{-0.9}$ | 17.7 $^{+1.1}_{-0.9}$ | 5290 | 4970 | 330 |
| PG 1411+442 | A | 1.5 \pm 0.1 | 11.9 $^{+0.5}_{-0.5}$ | 0.4 $^{+0.3}_{-0.1}$ | 1.2 $^{+0.3}_{-0.1}$ | 3.4 $^{+0.2}_{-0.1}$ | 2540 | 2270 | 220 |

^aAs defined in Paper I and Sulentic et al. (2000a)

^bRest-frame specific continuum flux at 1700 \AA in units of $10^{-14} \text{ erg s}^{-1} \text{ cm}^{-2} \text{ \AA}^{-1}$.

^cRest-frame line flux of CIII λ 1909, SiIII λ 1892, AlIII λ 1860 and of the CIV λ 1549 BC in units of $10^{-13} \text{ erg s}^{-1} \text{ cm}^{-2}$.

^dRest frame FWHM of the H β BC. UV is for SiIII λ 1892, AlIII λ 1860 and of the CIV λ 1549 BC in units of km s^{-1} .

Table 2. Derived Products*

| Object name (1) | $n_{\text{H}}U$ | | | | r_{BLR} | | | |
|--------------------|---|---|--|---|---------------------|---|---|---|
| | $c\cdot\tau$ (2) | $Aliii/Siii]$ (3) | $Ciii]/Siii]$ (4) | corr. (5) | $c\cdot\tau$ (6) | $Aliii/Siii]$ (7) | $Ciii]/Siii]$ (8) | corr. (9) |
| AKN 120 | 9.86 ^{+0.11} _{-0.08} | 9.70 ^{+0.22} _{-0.12} | 8.17 ^{+0.07} _{-0.03} | 10.44 ^{+0.36} _{-0.21} | 17.01 | 17.08 ^{+0.22} _{-0.13} | 17.85 ^{+0.08} _{-0.05} | 16.72 ^{+0.36} _{-0.22} |
| Fairall 9 | 10.55 ^{+0.19} _{-0.15} | 9.55 ^{+0.11} _{-0.10} | 7.99 ^{+0.03} _{-0.06} | 9.92 ^{+0.12} _{-0.12} | 16.65 | 17.15 ^{+0.12} _{-0.11} | 17.93 ^{+0.06} _{-0.08} | 16.97 ^{+0.13} _{-0.13} |
| MRK 335 | 10.39 ^{+0.20} _{-0.17} | 9.94 ^{+0.14} _{-0.13} | 7.91 ^{+0.08} _{-0.09} | 9.68 ^{+0.15} _{-0.14} | 16.61 | 16.83 ^{+0.15} _{-0.14} | 17.84 ^{+0.09} _{-0.10} | 16.96 ^{+0.16} _{-0.15} |
| MRK 509 | 10.34 ^{+0.07} _{-0.07} | 9.90 ^{+0.10} _{-0.11} | 8.09 ^{+0.10} _{-0.07} | 10.21 ^{+0.21} _{-0.16} | 16.82 | 17.03 ^{+0.10} _{-0.12} | 17.94 ^{+0.11} _{-0.08} | 16.89 ^{+0.21} _{-0.17} |
| NGC 3516 | 10.08 ^{+0.39} _{-0.61} | 9.60 ^{+0.10} _{-0.07} | 8.20 ^{+0.04} _{-0.02} | 10.15 ^{+0.18} _{-0.10} | 16.24 | 16.47 ^{+0.10} _{-0.08} | 17.17 ^{+0.05} _{-0.04} | 16.21 ^{+0.18} _{-0.10} |
| NGC 3783 | 10.11 ^{+0.18} _{-0.24} | 10.15 ^{+0.07} _{-0.11} | 8.07 ^{+0.26} _{-0.11} | 9.97 ^{+0.19} _{-0.13} | 16.42 | 16.39 ^{+0.07} _{-0.12} | 17.43 ^{+0.26} _{-0.11} | 16.49 ^{+0.20} _{-0.13} |
| NGC 5548 | 9.58 ^{+0.03} _{-0.03} | 9.93 ^{+0.12} _{-0.10} | 8.30 ^{+0.03} _{-0.02} | 10.15 ^{+0.19} _{-0.15} | 16.67 | 16.48 ^{+0.12} _{-0.11} | 17.30 ^{+0.05} _{-0.04} | 16.38 ^{+0.20} _{-0.15} |
| NGC 7469 | 10.91 ^{+0.14} _{-0.13} | 9.83 ^{+0.08} _{-0.06} | 7.90 ^{+0.05} _{-0.03} | 10.41 ^{+0.17} _{-0.12} | 16.07 | 16.60 ^{+0.09} _{-0.07} | 17.56 ^{+0.07} _{-0.06} | 16.32 ^{+0.18} _{-0.13} |
| PG 0052+251 | 9.94 ^{+0.21} _{-0.21} | 9.64 ^{+0.16} _{-0.14} | 8.07 ^{+0.06} _{-0.09} | 9.81 ^{+0.31} _{-0.21} | 17.37 | 17.51 ^{+0.17} _{-0.15} | 18.29 ^{+0.07} _{-0.09} | 17.43 ^{+0.31} _{-0.21} |
| PG 0953+414 | 9.73 ^{+0.12} _{-0.12} | 10.49 ^{+0.25} _{-0.17} | 8.24 ^{+0.39} _{-0.28} | ... | 17.59 | 17.20 ^{+0.26} _{-0.17} | 18.33 ^{+0.40} _{-0.28} | ... |
| PG 1211+143 | 9.45 ^{+0.32} _{-0.21} | 10.00 ^{+0.21} _{-0.17} | 8.17 ^{+0.20} _{-0.21} | 9.95 ^{+0.35} _{-0.24} | 17.39 | 17.10 ^{+0.22} _{-0.18} | 18.02 ^{+0.21} _{-0.22} | 17.14 ^{+0.35} _{-0.24} |
| PG 1307+085 | 9.63 ^{+0.32} _{-0.25} | 9.77 ^{+0.22} _{-0.29} | 8.17 ^{+0.13} _{-0.07} | 9.76 ^{+0.44} _{-0.35} | 17.44 | 17.36 ^{+0.22} _{-0.29} | 18.16 ^{+0.13} _{-0.08} | 17.37 ^{+0.44} _{-0.35} |
| PG 1411+442 | 9.01 ^{+0.35} _{-0.35} | 9.87 ^{+0.22} _{-0.31} | 7.53 ^{+0.21} _{-0.09} | 9.41 ^{+0.50} _{-0.36} | 17.51 | 17.07 ^{+0.22} _{-0.31} | 18.24 ^{+0.22} _{-0.10} | 17.31 ^{+0.50} _{-0.36} |

(*) $c\cdot\tau$ is derived from RM data. The $Aliii/Siii]$ ratio represents the high density solution, while the $Ciii]/Siii]$ ratio is the low density solution (see section 4). *corr.* is the correction due systematic effects (see section 4.1)

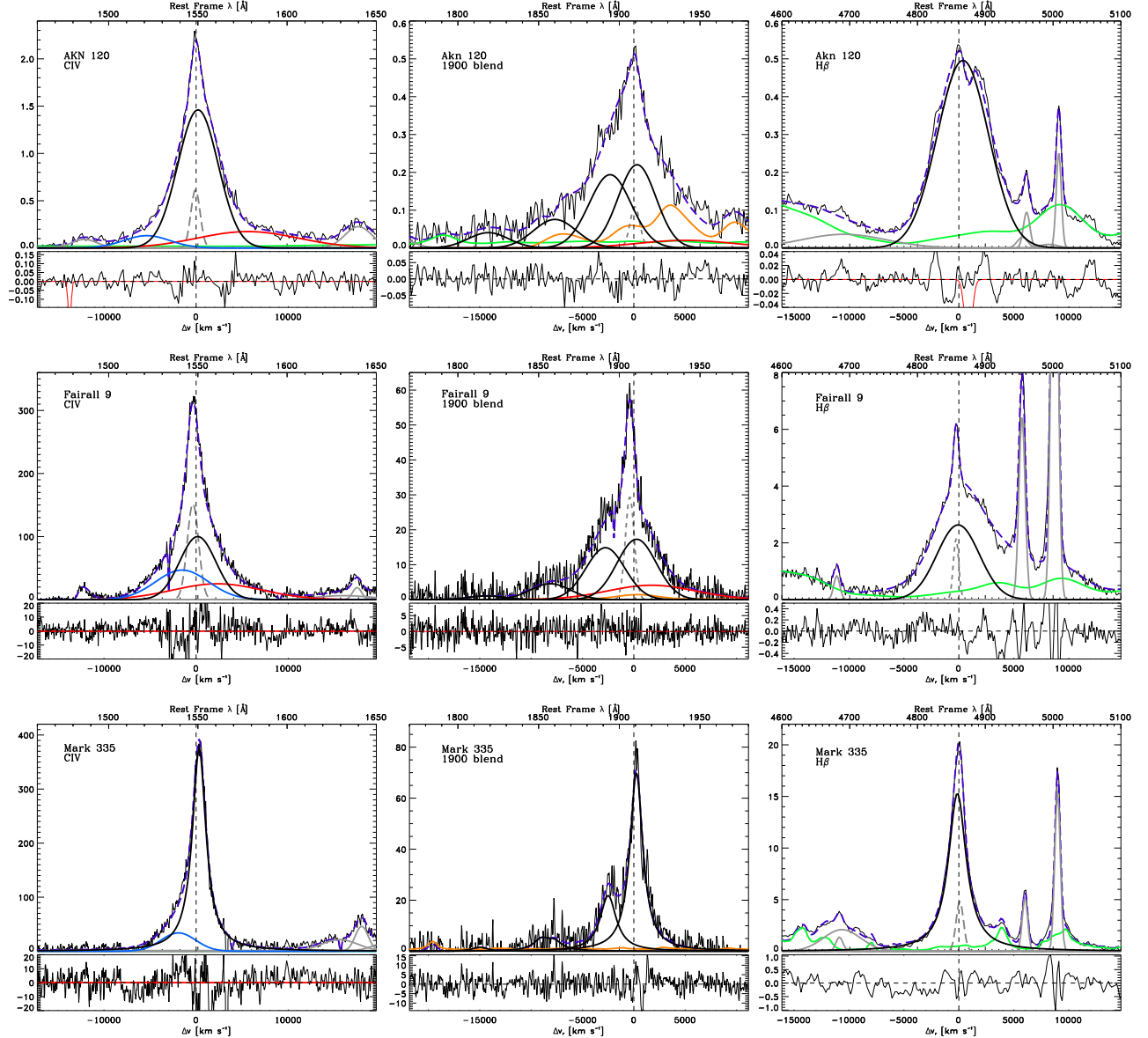


Fig. 1.— Multicomponent fits for the 13 objects of our sample. Upper abscissa is rest frame wavelength in \AA , lower abscissa is in radial velocity units, ordinate is specific flux per unit wavelength in arbitrary units. Panels under the fits are the residuals. Vertical long dashed line is the rest frame for (left) $\text{CIV}\lambda 1549$, (middle) $\text{CIII}\lambda 1909$ and (right) $\text{H}\beta$. Short purple dashed line is the fit to the whole spectrum. Black lines are the broad central components. Green lines represent the FeII template emission. The red lines are the VBC. The dashed grey lines are narrow components. The blue line in $\text{CIV}\lambda 1549$ corresponds to the BLUE component. The solid grey lines in $\text{H}\beta$ and $\text{CIV}\lambda 1549$ represents the contribution of various underlying weaker emission lines. The orange line in the $\lambda 1900\text{\AA}$ blend is the FeIII template. In the panels of the residuals, the thin red lines are absorption lines considered in the fits.

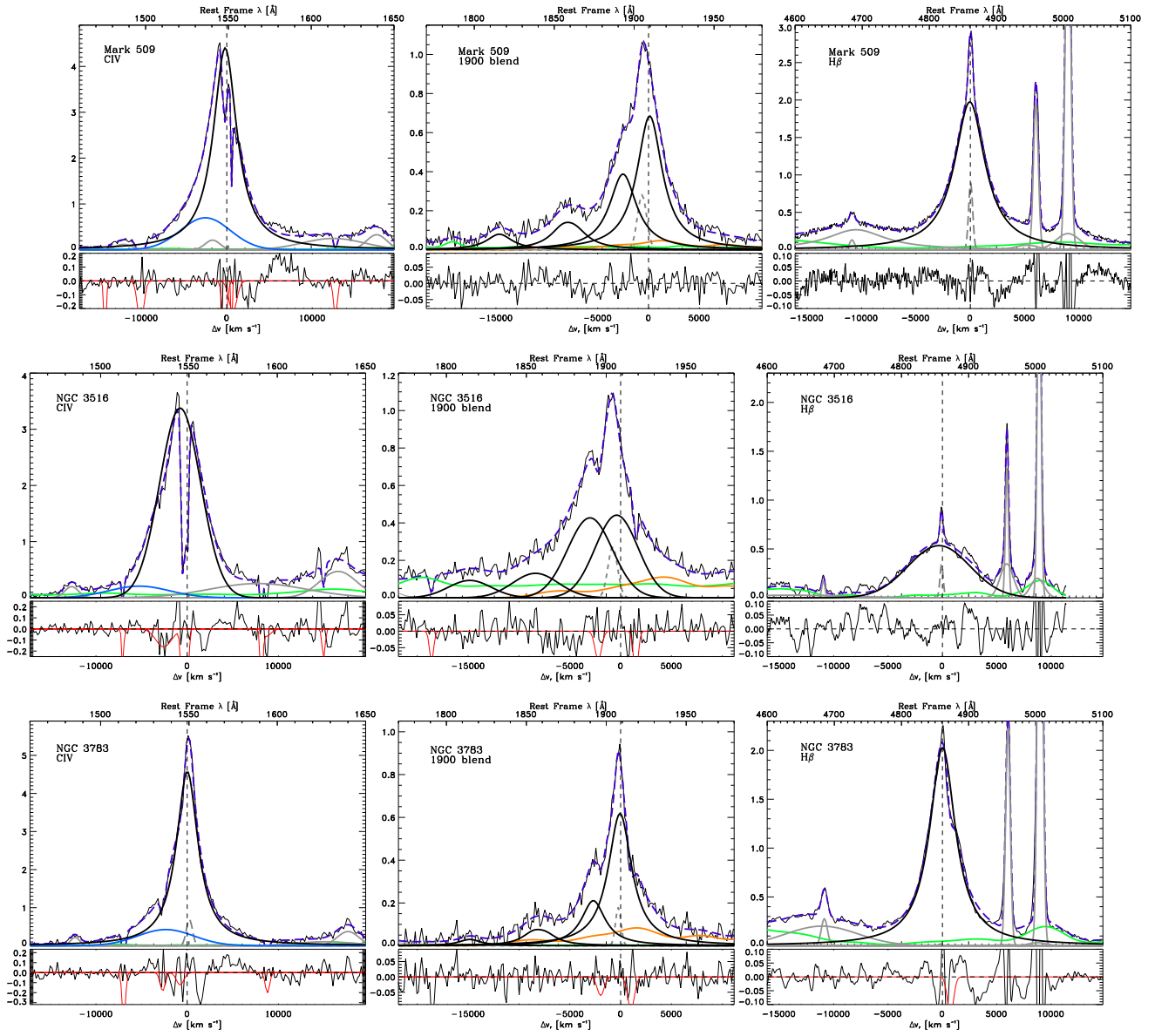


Fig. 1. — Continued.

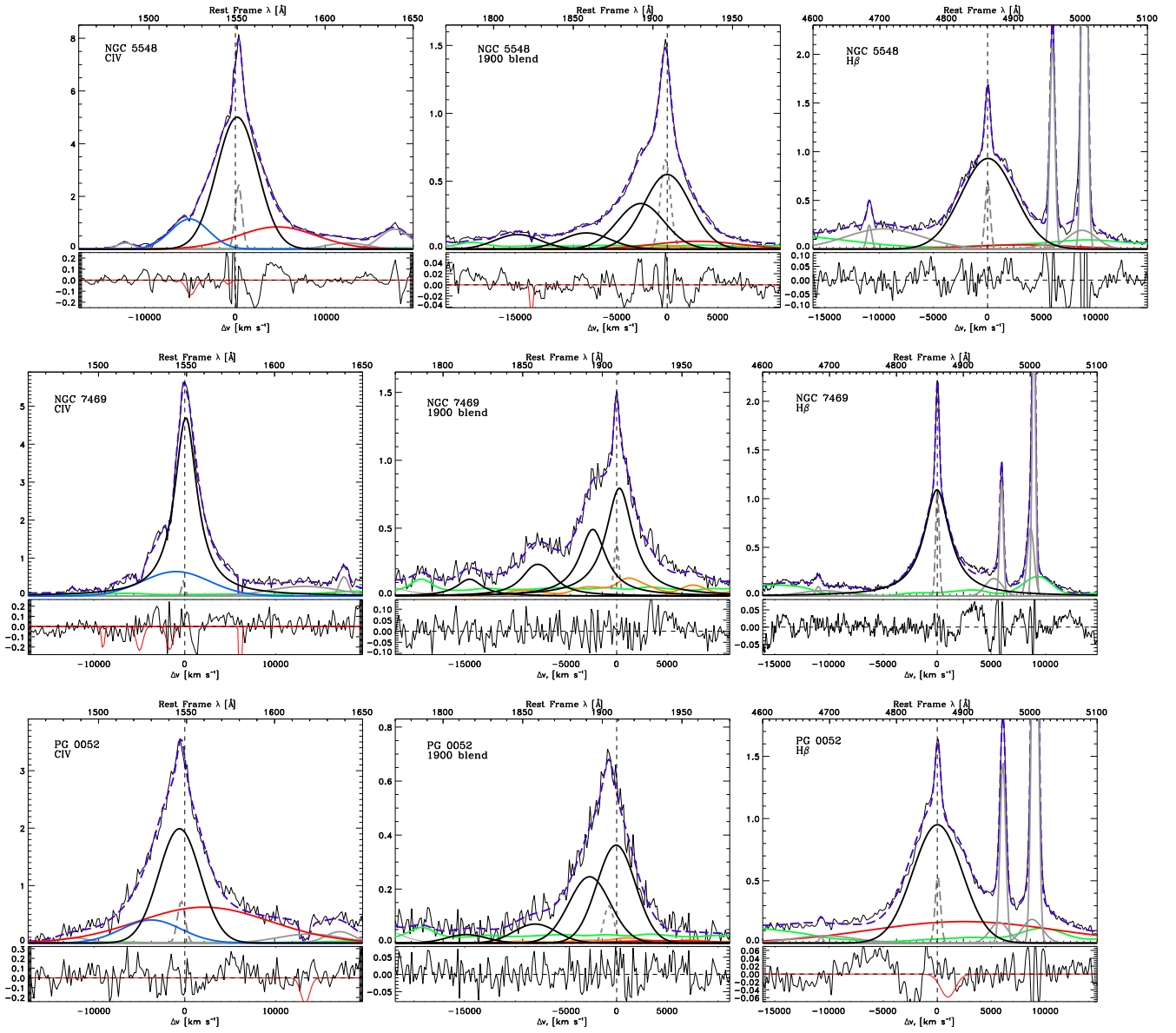


Fig. 1. — Continued.

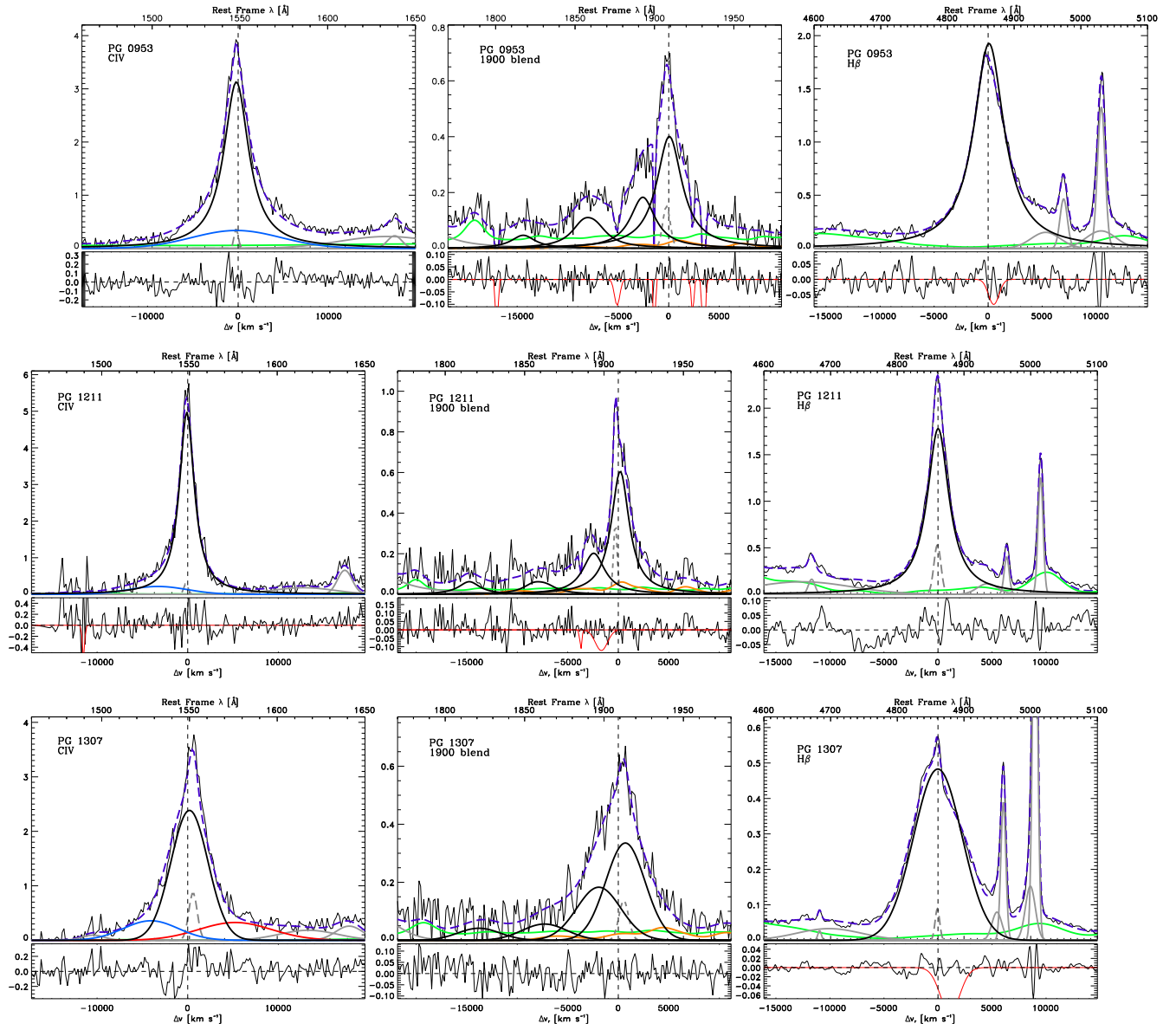


Fig. 1. — Continued.

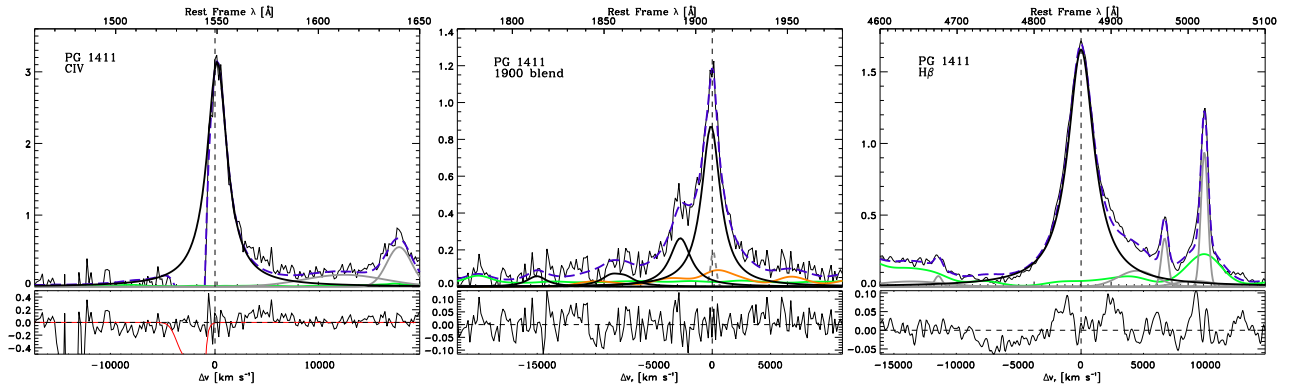


Fig. 1. — Continued.

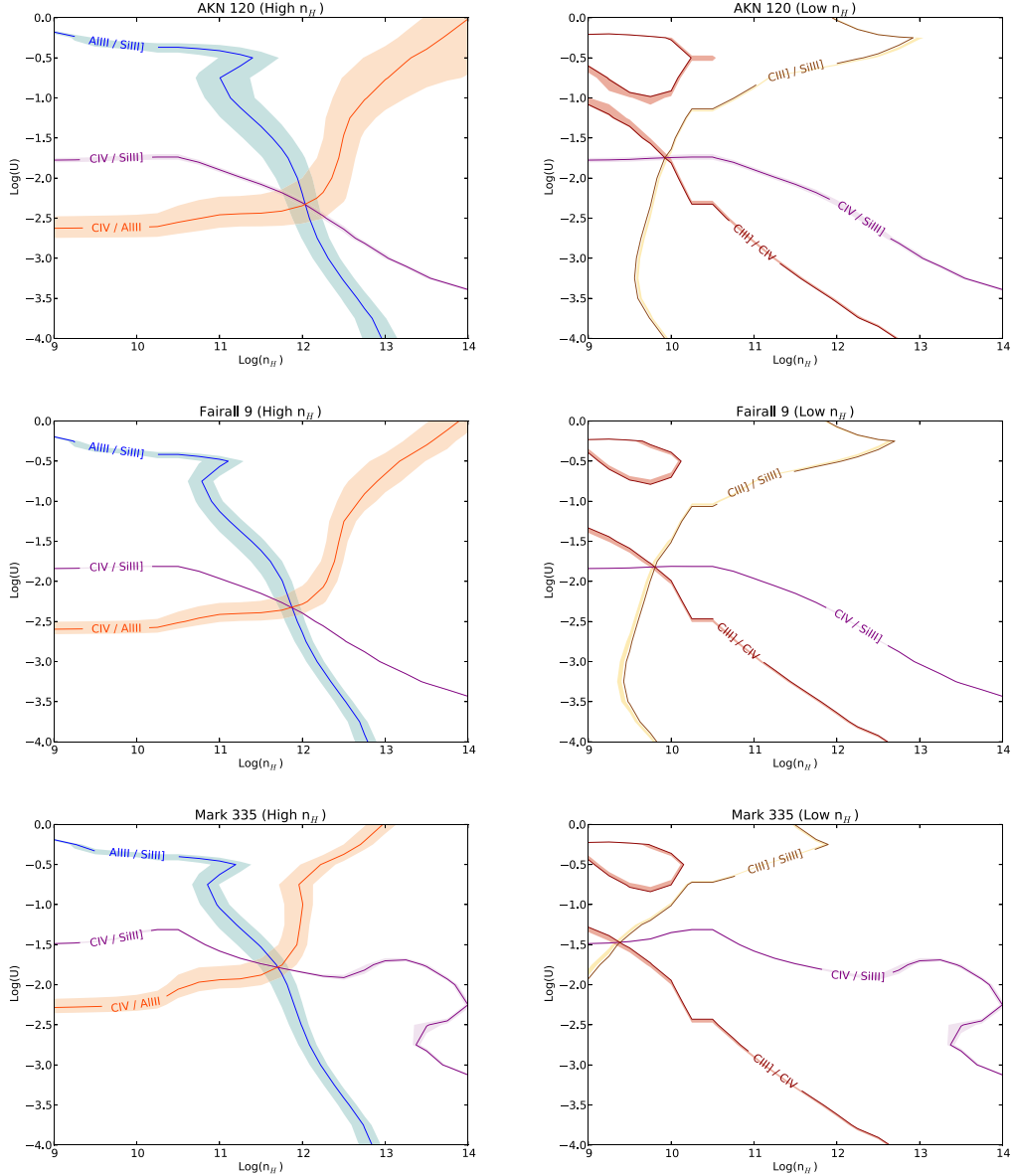


Fig. 2.— Identification of the “solutions” in the plane (n_H, U) . Abscissa is n_H in cm^{-3} , ordinate is the ionization parameter, both in logarithm scale. Left panels are the high density solution. Right panels are the low density solution. The point where the isocontours cross determine the values of $\log n_H + \log U$. The width of the isocontours are 1σ confidence.

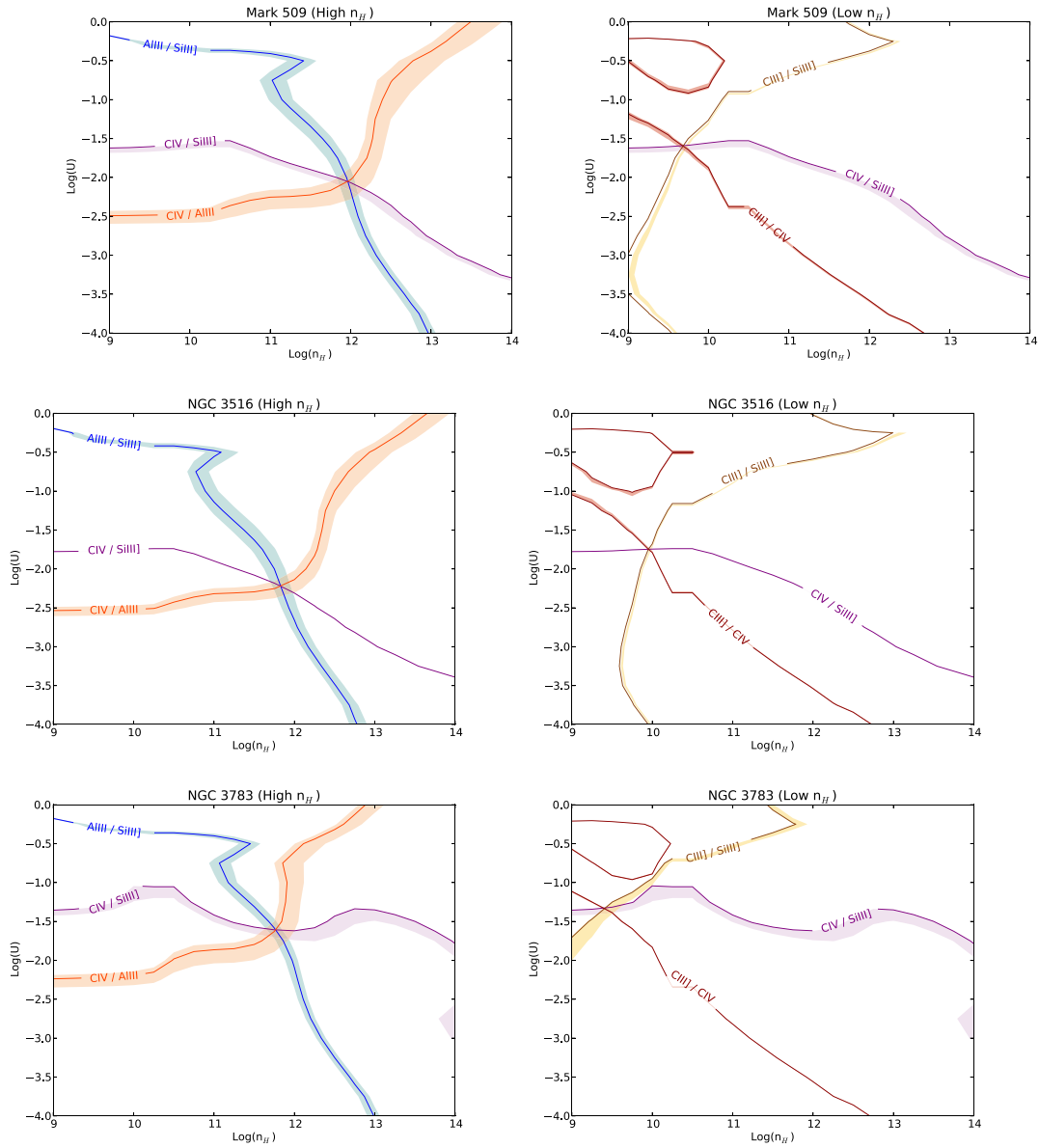


Fig. 2. — Continued.

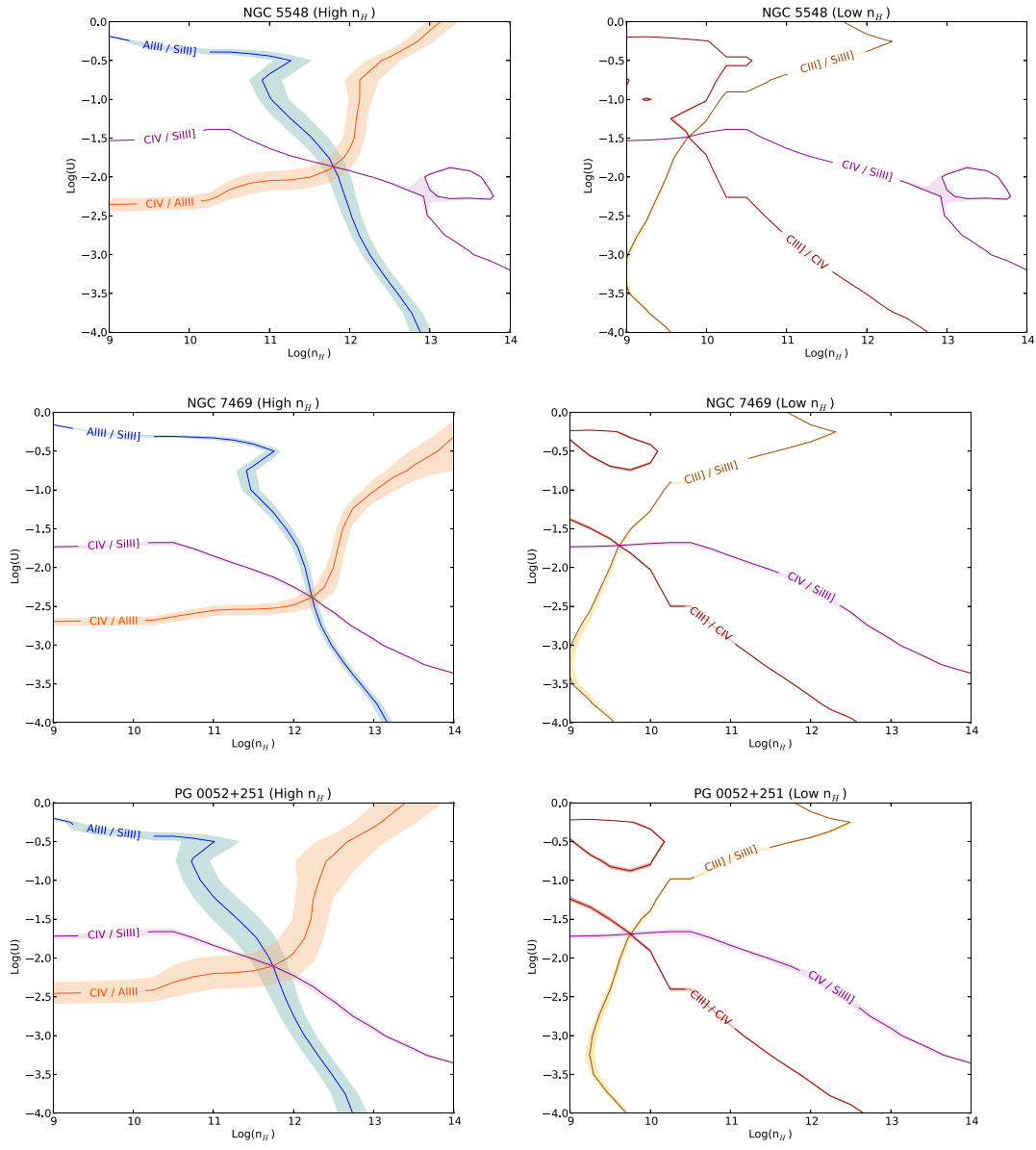


Fig. 2. — Continued.

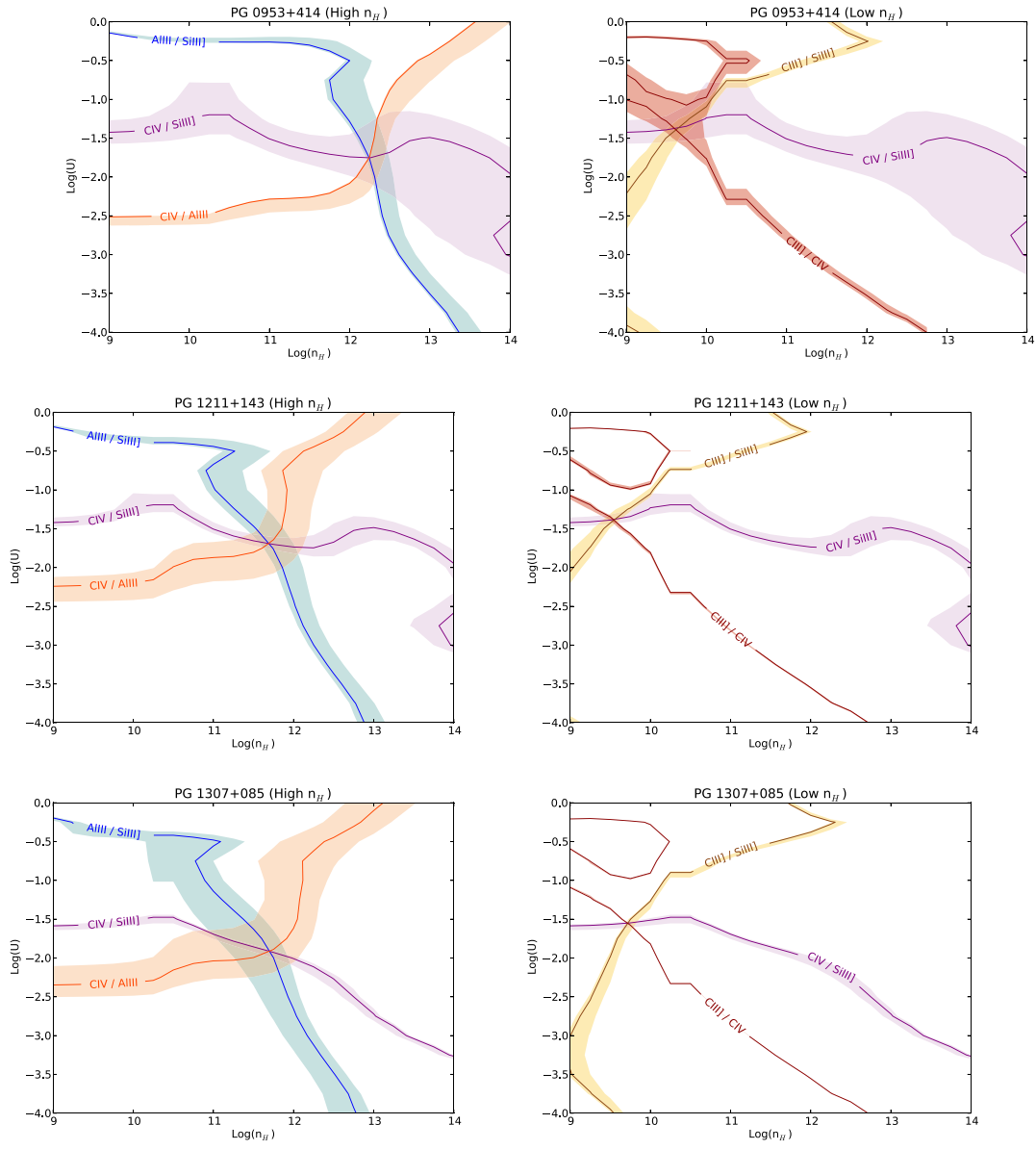


Fig. 2. — Continued.

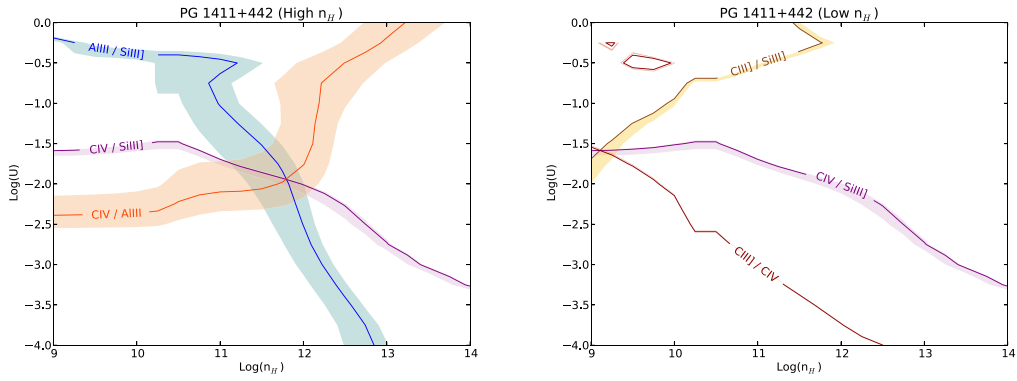


Fig. 2. — Continued.

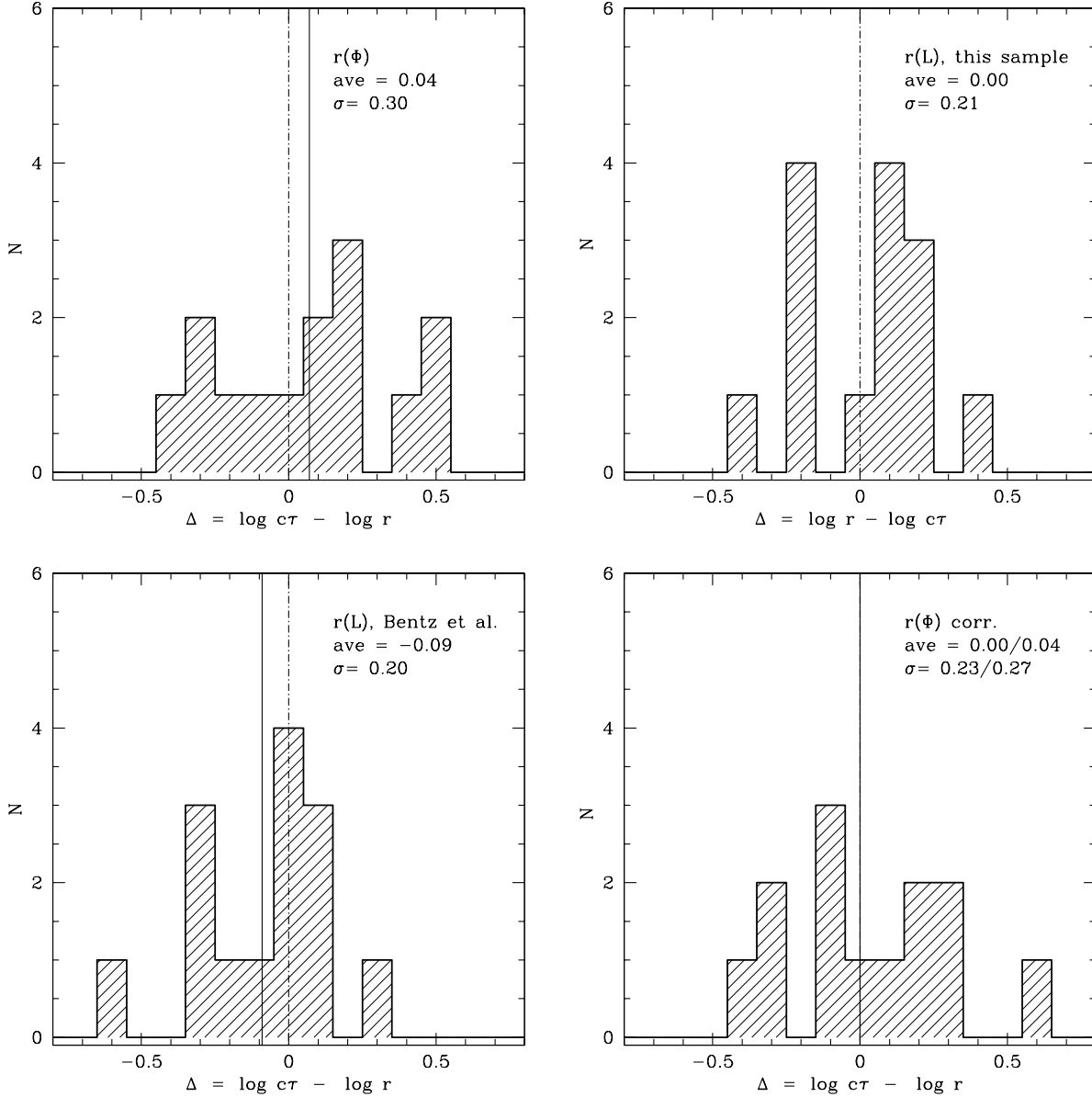


Fig. 3.— Residuals Δ between the reverberation based distance and r_{BLR} with 4 different method. (upper left) r_{BLR} with the photoionization method; (upper right) r_{BLR} with the luminosity correlation defined on the present sample; (lower left) r_{BLR} with the luminosity correlation of Bentz et al. (2009); (lower right) r_{BLR} with the photoionization method after correcting for a systematic effects dependent on the ratio $W(\text{AlIII}\lambda 1860)/W(\text{CIII}\lambda 1909)$. The two values in the lower right panel refer to the average and rms excluding/including PG 0953+414.

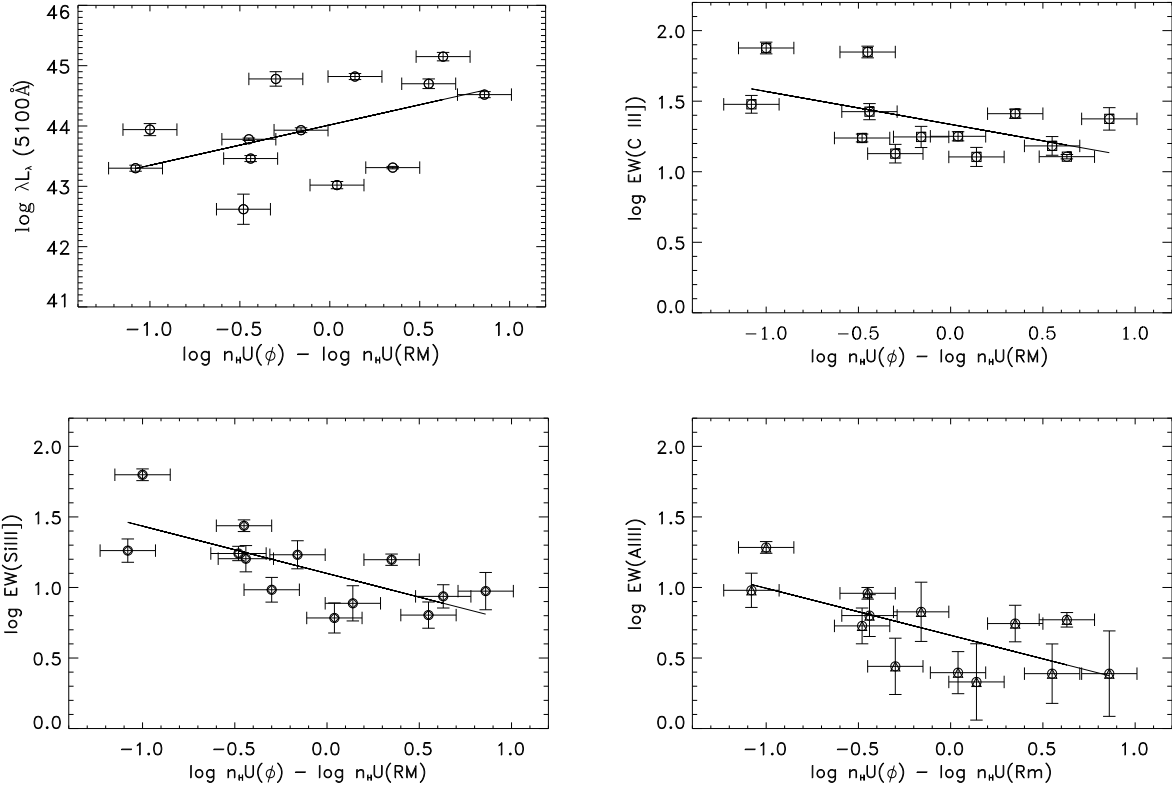


Fig. 4.— Difference $\Delta n_H U$ as a function of luminosity, $W(C III] \lambda 1909)$, $W(Al III] \lambda 1860)$ and $W(Si III] \lambda 1892)$. The filled line shows a least square fit.

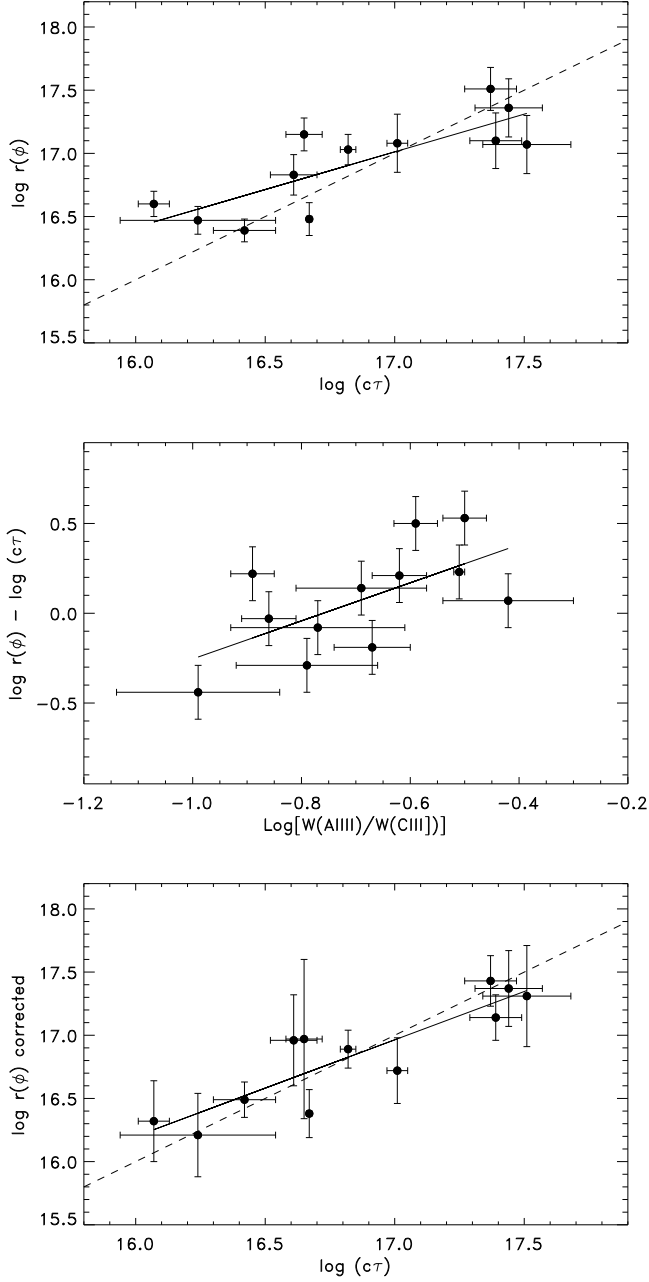


Fig. 5.— r_{BLR} comparison. Upper panel: $\log r_{\text{BLR}}(\phi)$ using the method of the present paper *vs.* the product $\log(c\tau)$ reported by Bentz et al. (2009). Middle panel: difference of distances Δr_{BLR} *vs.* $\log W(\text{AlIII}\lambda 1860)/W(\text{CIII}\lambda 1909)$. Lower panel: $\log r_{\text{BLR}}(\phi)$ corrected by the $W(\text{AlIII}\lambda 1860)/W(\text{CIII}\lambda 1909)$ ratio *vs.* $\log(c\tau)$. The dashed line shows equality; the filled line shows the result of a least square fit.

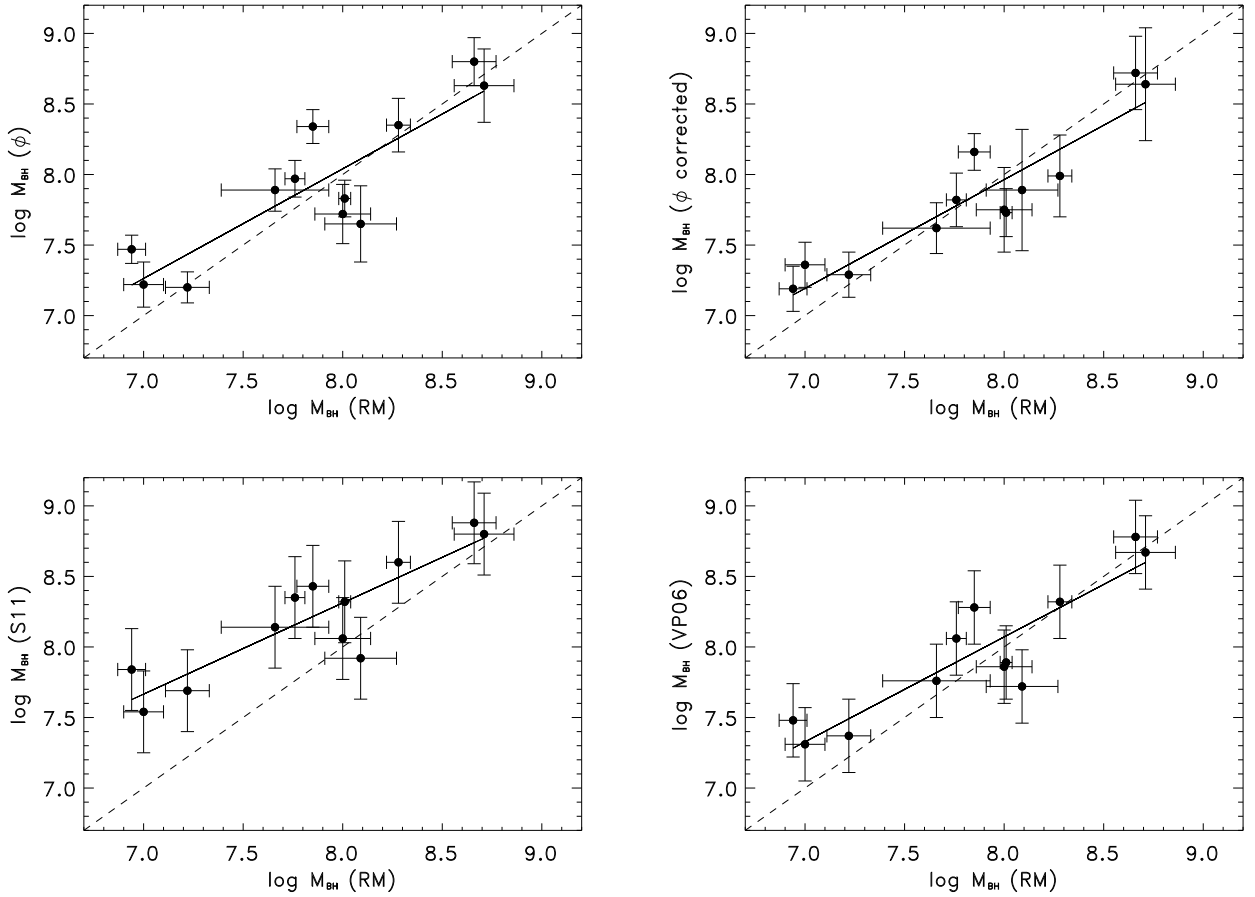


Fig. 6.— Comparison between masses derived using the reverberation mapping distance, and derived from the photoionization method (Φ , upper panels). Lower panels show two luminosity correlations. We consider 12 sources of this work. Upper right: uncorrected Φ ; upper left: Φ corrected for systematic effects on the basis of the $W(\text{AlIII}\lambda 1860)/W(\text{CIII}\lambda 1909)$ ratio; lower left: relation with M_{BH} computed following Shen et al. (2011); lower right: relation with M_{BH} computed following Vestergaard & Peterson (2006). The dashed line shows equality; the filled line shows the result of a least square fit.